Applied Thermal Engineering 212 (2022) 118600

Contents lists available at ScienceDirect

Applied Thermal Engineering

journal homepage: www.elsevier.com/locate/apthermeng

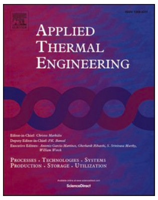

Research Paper

An isogeometric boundary element method for transient heat transfer problems in inhomogeneous materials and the non-iterative inversion of loads

Bo Yu [a,b,*], Geyong Cao [a], Shanhong Ren [a], Yanpeng Gong [c], Chunying Dong [d]

[a] Institute of Applied Mechanics, School of Civil Engineering, Hefei University of Technology, Hefei 230009, PR China
[b] State Key Laboratory of Structural Analysis for Industrial Equipment, Dalian University of Technology, Dalian 116024, PR China
[c] Institute of Electronics Packaging Technology and Reliability, Faculty of Materials and Manufacturing, Beijing University of Technology, Beijing 100124, PR China
[d] Department of Mechanics, School of Aerospace Engineering, Beijing Institute of Technology, Beijing 100081, PR China

ARTICLE INFO

Keywords:
Isogeometric dual reciprocity BEM
Multi-patch modeling
Non-iterative inversion method
Identification of boundary conditions
Precise integration method

ABSTRACT

In this paper, the transient thermal analysis theory of isogeometric dual reciprocity boundary element method (IG-DRBEM) of the multi-patch inhomogeneous complex model is established and the non-iterative inversion method of load identification is proposed based on the IG-DRBEM. The establishment of the multi-patch analysis theory framework extended the ability of IG-DRBEM to analyze complex geometry to some extent. The multi-patch analysis method adopted herein is simple and operable, and still retains the advantages of seamless connection between CAD generated geometry and response analysis of isogeometric boundary element method (IGBEM), which is very beneficial to expand IG-DRBEM to practical engineering application fields in the future. The inversion method based on IG-DRBEM makes full use of the good geometrical and field representation ability of NURBS, and further expands the application scope of IG-DRBEM. Furthermore, the introduction of the precision integration method for both forward and inverse problems improves the accuracy and stability of calculation to a certain extent. The numerical results show that the proposed method has good stability and accuracy even when solving complex geometric problems such as a fighter model. Moreover, the implementation of basis function expansion and regularization scheme further improves the accuracy and noise resistance of boundary condition inversion.

1. Introduction

Since the concept of isogeometric analysis was proposed in 2005 [1], many isogeometric numerical methods have been presented, such as the isogeometric finite element method (IGFEM) [2,3,4], the isogeometric collocation methods [5,6], the isogeometric boundary element method (IGBEM) [7,8], the isogeometric finite strip method [9], where the IGBEM really realized the seamless connection from CAD modeling to CAE analysis because the boundary element method (BEM) only needs to discretize boundary. Up to now, the IGBEM has been significantly developed to solve elastostatic [7,10,11], acoustic [12,13,14], potential problems [15,16], electromagnetic scattering [17,18], steady heat transfer analysis [19], fatigue crack growth [20,21], structural shape optimization [8,22,23], elasto-plastic inclusions [24], topology optimization [25,26], and thermoelastic problems [23,27]. It is noteworthy that these study works are time-independent, whereas the practical engineering problems are mostly time-related. Due to the limitation of the fundamental solution, the transient problem involves the transformation of the domain integral when using BEM. And the discretization of the domain will destroy the dimension reduction and precision advantage of BEM's "boundary-only". So, the research on IGBEM at present seldom focuses on transient problems. In 2021, Yu et al. [28] and Xu et al. [29] proposed respectively the isogeometric dual reciprocity boundary element method (IG-DRBEM) and the radial integration isogeometric boundary element method (RI-IGABEM) to realize the solution of transient heat conduction problem, where the classical dual reciprocity BEM and the radial integral method are applied to transform the domain integral as boundary integral. Although these two IGBEM time-domain methods can accurately solve the transient problems, the solving models are composed of the simple single-patch models. To promote the adaptability of IG-DRBEM to solving problems with

---

* Corresponding author at: Institute of Applied Mechanics, School of Civil Engineering, Hefei University of Technology, Hefei 230009, PR China.
E-mail address: yubochina@hfut.edu.cn (B. Yu).

https://doi.org/10.1016/j.applthermaleng.2022.118600
Received 18 December 2021; Received in revised form 30 March 2022; Accepted 28 April 2022

Nomenclature

c	specific heat
g	heat source
k	thermal conductivity
N_b	number of boundary collocation points
N_I	number of interior points
N_t	the total number of boundary and interior points
q	heat flux
t	time
T	temperature
$\widetilde{T}$	the normalized temperature
$\boldsymbol{x} = \boldsymbol{x}(x_1, x_2, x_3)$	spatial coordinate
J	error function
$\widetilde{\boldsymbol{T}}$	the normalized temperature expansion coefficients of control points
ρ	density
λ	regularization parameter
β	shrinkage coefficient
Δt	time step

Abbreviations

IG-DRBEM	isogeometric dual reciprocity boundary element method
PIM	precise integral method

complex geometries and facilitate the procedure of modeling, the multi-patch analysis method should be considered urgently.

So far, there are many IGFEM based multi-patch processing schemes that have been elaborated, such as Nitsche's method [30,31] with trimmed elements [32] and overlapping multi-patch (OMP) [33] method for analyzing multiple overlap geometries. However, little IGBEM literature concerns multi-patch modeling theory. For instance, Wang et al. [34] based on the trimmed elements established the multi-patch nonsingular IGBEM in 2015. In the same year, Wang and Benson [35] proposed a considerable new collocation method which moves the first and the last collocation points of each parametric direction inside of their patches. This approach to deal with multi-patch modeling is simple and practical, which is similar to the idea of traditional BEM to deal with corner points. By adopting the effective collocation scheme in [35], the IG-DRBEM theory of three-dimensional inhomogeneous functionally graded materials (FGMs) proposed by Yu et al. [36] is firstly extended to enable the analysis of multi-patch models.

Another important problem is that the literature [36] uses a two-level time integration scheme to solve the time-domain problem. Though accurate solutions can be obtained by using this method, the results are greatly sensitive to the change of time step, so different time steps often lead to different results. Meanwhile, the two-level time integration scheme usually requires smaller time steps to ensure precision, which undoubtedly increases the calculation burden of both forward and inverse problems. It is worth noting that Yu et al. [37] in 2014 coupled the precise integral method (PIM) with the radial integral BEM for the first time to solve the transient heat transfer, and the numerical results showed that the PIM could obtain very stable numerical results. Especially when the time integral term can be calculated analytically, the time-domain solution will completely not be influenced by the size of the time step. Despite the numerical accuracy in [37] being satisfactory, the integration of CAD and CAE was not realized because the boundary element discrete processing is still needed before computation. And different from the radial integration method which requires complex mathematical derivation and computer programming, the dual reciprocity method (DRM) [38] utilizes the same BEM fundamental solution as the steady-state homogeneous problem. Thereby, DRM has a more concise matrix structure and is convenient to achieve.

Before the execution of inverse analysis, an appropriate method for the forward problem is well known to be the premise of high precision inversion. After decades of research, FEM and BEM have been some of the most popular inverse problem foundations. Particularly Kefal et al. have made outstanding contributions to the dynamic features and shape sensing of thin shells and composite structures by inverse FEM (iFEM) in recent years. In 2020, Kefal [39] and his collaborators developed an isogeometric finite element–boundary element method for calculating the hydroelastic vibration response of the partially filled horizontal cylindrical shell and achieved a perfect agreement with the experimental results. In the same year, Kefal and Oterkus [40] implemented real-time displacement field reconstruction of thin shell structures based on weighted least squares variational theory by using the isogeometric iFEM with Kirchhoff–Love inverse-shell element. This work introduced IGA to simplify the modeling and accurately represented geometry while reducing the number of strain sensors required. Then, by means of coupled iFEM and smooth element analysis, Kelfa et al. [41] extended the displacement reconstruction methodology to composite structures in 2021. Experimental results show that this method has excellent shape sensing ability under the condition of further reducing the number of sensors. Similarly, Zhao et al. [42,43] in 2021 successfully reconstructed the displacement fields of wings and composite sandwich beams by coupling IGA and iFEM with Refined Zigzag theory. But under the environment of the 3D transient heat conduction of FGMs, the proposed method of this paper considers establishing a multi-patch IG-DRBEM methodology in the forward problem which is based on the IGBEM with the characteristics of automatic discrete elements and dimension reduction analysis. The system of ordinary differential equations is formed by transforming domain integrals through the convenient DRM. Then, PIM is introduced under IGA to stabilize the results of the time-domain problem calculations. In addition, the multi-patch collocation scheme ensures the NURBS model can be built flexibly and easily. On account of this, the multi-patch IG-DRBEM based on PIM is expected to lay a solid foundation for accurate and efficient determination of variables to be identified. Consequently, the IG-DRBEM herein will be extended to the solution of the inverse problem for the first time.

Different from the forward heat transfer problem, identifying the geometric shape [44], boundary conditions [45,46], initial conditions [47], physical parameters [48] and the heat source [49] by means of some known thermal responses of measuring points are so-called inverse heat transfer problems. In respect of the practical application, especially in the aerospace [50], nuclear industry [51] and other cutting-edge technology fields. It is a crucial step to accurately know the real-time thermal loads of components in normal operation for reasonable structural design and appropriate material selection, so as to ensure safe and effective work. Nevertheless, due to the constraints of measurement techniques and environmental factors, the measurement values of loads cannot be directly obtained in many cases. Hence, identifying the unknown load by the easily measured responses is quite meaningful. The present work focuses on the inversion of boundary unknown time-varying temperature and heat flux of FGMs. In general, the inversion methods of boundary conditions according to the inversion process can be divided into two categories: iterative method and non-iterative method. However, when the iterative method is adopted to identify loads, the forward problem needs to be called many times. To improve the inversion efficiency, it is very significant to study the non-iterative inversion method. In this respect, Tamburrino et al. [52] presented a non-iterative inversion method based on the monotonicity of the resistance matrix. Ling et al. [53] proposed a non-iterative inverse method based on the finite element method for estimating surface heat flux histories on thermally conducting bodies. Recently, Yu et al. [54,55] based on the least square method proposed a non-iterative inversion method for identifying the unknown boundary condition and the unknown geometry. The works in [54,55] have made great contributions to the research of the inverse heat transfer problem, but it still needs to be promoted. For example, the literature [54] solved the boundary condition identification problem of steady-state heat conduction based on traditional BEM, but the ill-posed level of the inverse problem was not well alleviated due to the failure of the basis function approximation and regularization treatment. And the algorithm did not involve inhomogeneous material problems and transient problems. Although the reference [55] adopted the precise integral finite element method (PIFEM) to deal with the transient heat transfer problem of FGMs and coupled the non-iterative method to carry out the inversion of boundary conditions and geometric shapes, the element discretization in the domain brought the loss of accuracy and efficiency to some extent in the analysis process. To this end, the study of the non-iterative inversion method for transient load identification based on the IG-DRBEM can realize the systematic solving of forward and inverse problems from CAD to CAE, and give full play to the advantages of high solving accuracy, easy pre-processing and high efficiency of non-iterative inversion method.

Moreover, when the load distribution region is wide, the number of nodes to be inverted will be large. In order to facilitate the precision and numerical stability of inversion results and reduce the cost of inversion calculation, Yu et al. [55] transformed the problem of load identification into the problem of solving a certain amount of undetermined coefficients by using the basis function expansion technique and adopted the Tikhonov regularization to advance the tolerance of inversion precision to measurement errors. These schemes will be considered herein to enhance the performance of the presented method.

The paper is organized as follows. The problem description is presented in Section 2. The solution of the forward problem is detailed introduced in Section 3. The inversion theory of boundary conditions is presented in Section 4. Several well-designed examples are discussed in Section 5. Finally, the main findings of the present work and some prospects are summarized in Section 6.

2. Governing equation

In this paper, the 3D transient heat conduction problem in FGMs is considered. The governing equation can be written as.

$$\frac{\partial}{\partial x_i}\left[k(\boldsymbol{x})\frac{\partial T(\boldsymbol{x},t)}{\partial x_i}\right]+g(\boldsymbol{x},t)=\rho(\boldsymbol{x})c(\boldsymbol{x})\frac{\partial T(\boldsymbol{x},t)}{\partial t},\quad \boldsymbol{x}\in\Omega\quad,\qquad (i=1,2,3) \tag{1}$$

where the repeated subscripts represent summation conventions, $T(\boldsymbol{x},t)$ and $g(\boldsymbol{x},t)$ are temperature and heat source functions of spatial coordinate $\boldsymbol{x}=\boldsymbol{x}(x_1,x_2,x_3)$ and time$t$, respectively; the thermal conductivity$k(\boldsymbol{x})$, the density $\rho(\boldsymbol{x})$ and the specific heat $c(\boldsymbol{x})$ are the function of the spatial coordinatex_i. Here, temperature and heat flux boundary conditions are considered as follows.

$$T(\boldsymbol{x},t)\ =\ \overline{T}(\boldsymbol{x},t)\ ,\qquad \boldsymbol{x}\in\Gamma_1 \tag{2}$$

and.

$$-k(\boldsymbol{x})\frac{\partial T}{\partial \boldsymbol{n}}\ =\ \overline{q}(\boldsymbol{x},t)\ ,\qquad \boldsymbol{x}\in\Gamma_2 \tag{3}$$

where$\Gamma_1\cap\Gamma_2=\varnothing,\Gamma_1\cup\Gamma_2=\Gamma$, Γ is the boundary of whole domainΩ, $\boldsymbol{n}$ is the outer normal vector, $\overline{T}$ and $\overline{q}$ are known functions of temperature and heat flux.

3. Solving the forward problem by IG-DRBEM

3.1. Discretizing of integral equation

In the literature [36], the IG-DRBEM has been detailly described for solving the single-patch modeling in FGMs. In this section, we focus on the process derivation of IG-DRBEM in multi-patch modeling. The detailed introduction of NURBS basis functions and the derivation process of boundary integral equation can be seen in the literature [36] Section 3 and 4, respectively. The boundary integral equation (Equation (17), in the literature [36]) applying DRBEM is given by.

$$\begin{aligned}&C(\boldsymbol{x}')\widetilde{T}(\boldsymbol{x}',t)+\int_\Gamma\widetilde{T}(\boldsymbol{x},t)q^*(\boldsymbol{x}',\boldsymbol{x})\mathrm{d}\Gamma-\int_\Gamma q(\boldsymbol{x},t)T^*(\boldsymbol{x}',\boldsymbol{x})\mathrm{d}\Gamma\\ &=\sum_{j=1}^{N_t}a_j\left[C(\boldsymbol{x}')\widehat{T}_j(\boldsymbol{x}')+\int_\Gamma\widehat{T}_j(\boldsymbol{x})q^*(\boldsymbol{x}',\boldsymbol{x})\mathrm{d}\Gamma-\int_\Gamma\widehat{q}_j(\boldsymbol{x})T^*(\boldsymbol{x}',\boldsymbol{x})\mathrm{d}\Gamma\right]\end{aligned} \tag{4}$$

where N_t denotes the boundary and interior points, $\widetilde{T}(\boldsymbol{x},t)$ is called the normalized temperature in which is given by$\widetilde{T}(\boldsymbol{x})\ =k(\boldsymbol{x})T(\boldsymbol{x},t)$, T^* is the fundamental solution of 3D potential problem, and$q(\boldsymbol{x})=k(\boldsymbol{x})\partial T/\partial\boldsymbol{n}$. The remaining variables in Eq. (4) can be explained in the Section 4.1 of literature [36].

Before the discretization of the integral equation, the matching scheme of the collocation points should be considered. In general, the Greville abscissae method [7] is used to generate the collocation points in parameter space. However, the scheme of generating collocation points can cause the ill-posed algebraic equations for multi-patch modeling. To circumvent this problem, an improved collocation scheme based on the literature [35] is proposed for solving complex geometry with multi-patch modeling in IG-DRBEM. The main idea of this procedure is to move collocation points on each patch from the boundary into the inside of the patch as shown in Fig. 1, in which each surface of the cube is a patch.

The corresponding obtained method of collocation points in parameter space $\left(\xi_i',\eta_j'\right)$ in the Greville abscissae method can be expressed as.

$$\begin{cases}\xi_i'=\dfrac{\xi_{i+1}+\xi_{i+2}+\ldots+\xi_{i+p}}{p} & i=1,2,\cdots,n\\[2ex] \eta_j'=\dfrac{\eta_{j+1}+\eta_{j+2}+\ldots+\eta_{j+q}}{q} & j=1,2,\cdots,m\end{cases} \tag{5}$$

where p and q are the order of NURBS basis functions, n and m are the number of control points on the directions ξ andη, respectively. To generate new collocation points in the parameter space, a shrinkage coefficient β is introduced to regenerate the first (subscript: 1) and last (subscript: *end*) parameter of collocation points as follows.

$$\begin{cases}\xi_1'=\xi_1'+\beta(\xi_2'-\xi_1'); & \xi_{end}'=\xi_{end}'-\beta(\xi_{end}'-\xi_{end-1}')\\ \eta_1'=\eta_1'+\beta(\eta_2'-\eta_1'); & \eta_{end}'=\eta_{end}'-\beta(\eta_{end}'-\eta_{end-1}')\end{cases} \tag{6}$$

To describe clearly, it is assumed that temperature and heat flux boundary conditions are respectively applied to the boundary Γ_1 andΓ_2, where Γ_1 and Γ_2 are distributed into N_{b1} and N_{b2} collocation points, respectively. The entire boundary is distributed into N_b collocation points i.e.$N_b\ =N_{b1}\ +N_{b2}$. Applying N_b boundary collocation points and N_I interior points to Eq. (4) and using NURBS to discretize the boundary integral equation, an system of ordinary differential equations (ODEs) can be obtained as follows.

$$\boldsymbol{ER}\frac{\partial\widetilde{\boldsymbol{T}}(t)}{\partial t}-(\boldsymbol{DR}-\boldsymbol{H})\widetilde{\boldsymbol{T}}(t)=\boldsymbol{Gq}(t)+\boldsymbol{Cg}(t) \tag{7}$$

where the detailed derivation of Eq. (7) and the generation process of the matrices$\boldsymbol{E}$,$\boldsymbol{R}$,$\boldsymbol{D}$,$\boldsymbol{H}$,$\boldsymbol{G}$, $\boldsymbol{C}$ can be seen in the literature [36].

Note that the vector $\widetilde{\boldsymbol{T}}$ includes the normalized temperature expansion coefficients of control points (NTECCP) $\widetilde{\boldsymbol{T}}_b=\left\{\{\widetilde{\boldsymbol{T}}_{b1}\}_{N_{b1}\times1}^{\mathrm{T}},\{\widetilde{\boldsymbol{T}}_{b2}\}_{N_{b2}\times1}^{\mathrm{T}}\right\}^{\mathrm{T}}$ and temperature of interior points$\widetilde{\boldsymbol{T}}_I$. Similarly, $\boldsymbol{q}$ is composed of the heat flux expansion coefficients of control points (HFECCP). Let $N_u=N_{b2}+N_I$ and$N_t\ =N_b+N_I$, the normalized temperature and heat flux vector can be expressed in the following block form.

$$\widetilde{\boldsymbol{T}}=\left\{\{\widetilde{\boldsymbol{T}}_{b1}\}_{N_{b1}\times1}^{\mathrm{T}},\{\widetilde{\boldsymbol{T}}_{b2}\}_{N_{b2}\times1}^{\mathrm{T}},\{\widetilde{\boldsymbol{T}}_I\}_{N_i\times1}^{\mathrm{T}}\right\}^{\mathrm{T}}=\left\{\{\widetilde{\boldsymbol{T}}_{b1}\}_{N_{b1}\times1}^{\mathrm{T}},\{\widetilde{\boldsymbol{T}}_u\}_{N_u\times1}^{\mathrm{T}}\right\}^{\mathrm{T}} \tag{8}$$

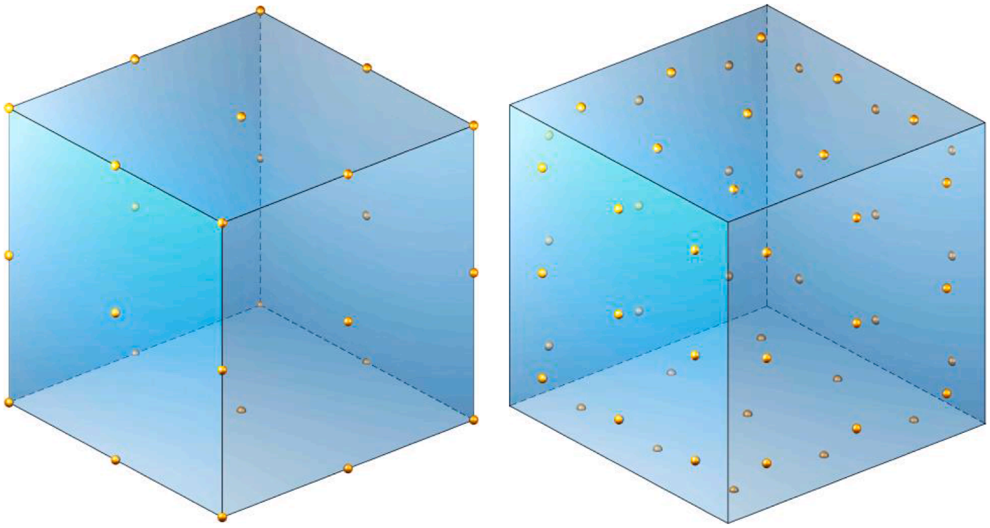

(a) Greville abscissae method (b) Improved collocation scheme

Fig. 1. Schematic diagram of multi-patch collocation points.

$$\boldsymbol{q}=\left\{\{\boldsymbol{q}_{b1}\}_{N_{b1}\times 1}^{\mathrm{T}},\{\boldsymbol{q}_{b2}\}_{N_{b2}\times 1}^{\mathrm{T}}\right\}_{N_b\times 1}^{\mathrm{T}} \tag{9}$$

After applying boundary conditions, the ODEs can be given as follows.

$$\widetilde{\boldsymbol{\psi}}\frac{\partial \widetilde{\boldsymbol{T}}}{\partial t}=\breve{\boldsymbol{\psi}}\boldsymbol{X}+\widehat{\boldsymbol{\psi}} \tag{10}$$

The matrices$\widetilde{\boldsymbol{\psi}}$, $\breve{\boldsymbol{\psi}}$ and the vectors$\widehat{\boldsymbol{\psi}}$, $\boldsymbol{X}$ can be written in the following block matrix form.

$$\widetilde{\boldsymbol{\psi}}=(\boldsymbol{ER})_{(N_t\times N_t)}=\begin{bmatrix}(\widetilde{\boldsymbol{\psi}}_{11})_{(N_{b1}\times N_{b1})} & (\widetilde{\boldsymbol{\psi}}_{12})_{(N_{b1}\times N_u)}\\(\widetilde{\boldsymbol{\psi}}_{21})_{(N_u\times N_{b1})} & (\widetilde{\boldsymbol{\psi}}_{22})_{(N_u\times N_u)}\end{bmatrix} \tag{11}$$

$$\begin{aligned}\breve{\boldsymbol{\psi}}&=\begin{bmatrix}\boldsymbol{G}_{(N_t\times N_{b1})} & (\boldsymbol{DR}-\boldsymbol{H})_{(N_t\times N_{b2})} & (\boldsymbol{DR}-\boldsymbol{H})_{(N_t\times N_I)}\end{bmatrix}\\&=\begin{bmatrix}(\breve{\boldsymbol{\psi}}_{11})_{(N_{b1}\times N_{b1})} & (\breve{\boldsymbol{\psi}}_{12})_{(N_{b1}\times N_u)}\\(\breve{\boldsymbol{\psi}}_{21})_{(N_u\times N_{b1})} & (\breve{\boldsymbol{\psi}}_{22})_{(N_u\times N_u)}\end{bmatrix}\end{aligned} \tag{12}$$

$$\widehat{\boldsymbol{\psi}}=(\boldsymbol{DR}-\boldsymbol{H})_{(N_t\times N_{b1})}\widetilde{\boldsymbol{T}}_{b1}+\boldsymbol{G}_{(N_t\times N_{b2})}\boldsymbol{q}_{b2}+\boldsymbol{C}_{(N_t\times N_t)}\boldsymbol{g}=\begin{bmatrix}(\widehat{\boldsymbol{\psi}}_1)_{(N_{b1}\times 1)}\\(\widehat{\boldsymbol{\psi}}_2)_{(N_u\times 1)}\end{bmatrix} \tag{13}$$

$$\boldsymbol{X}=\left\{\{\boldsymbol{q}_{b1}\}_{(N_{b1}\times 1)}^{\mathrm{T}},\{\widetilde{\boldsymbol{T}}_{b2}\}_{(N_{b2}\times 1)}^{\mathrm{T}},\{\widetilde{\boldsymbol{T}}_I\}_{(N_I\times 1)}^{\mathrm{T}}\right\}^{\mathrm{T}}=\backslash\{\ \{\boldsymbol{q}_{b1}\}_{(N_{b1}\times 1)}^{\mathrm{T}},\{\widetilde{\boldsymbol{T}}_u\}_{(N_u\times 1)}^{\mathrm{T}}\backslash\}^{\mathrm{T}} \tag{14}$$

where.

$$\begin{cases}\widehat{\boldsymbol{\psi}}_1=(\boldsymbol{DR}-\boldsymbol{H})_1\widetilde{\boldsymbol{T}}_{b1}+\boldsymbol{G}_1\boldsymbol{q}_{b2}+\boldsymbol{C}_1\boldsymbol{g}\\\widehat{\boldsymbol{\psi}}_2=(\boldsymbol{DR}-\boldsymbol{H})_2\widetilde{\boldsymbol{T}}_{b1}+\boldsymbol{G}_2\boldsymbol{q}_{b2}+\boldsymbol{C}_2\boldsymbol{g}\end{cases} \tag{15}$$

The matrix blocks$(\boldsymbol{DR}-\boldsymbol{H})_1$,$(\boldsymbol{DR}-\boldsymbol{H})_2$,$\boldsymbol{G}_1$,$\boldsymbol{G}_2$, $\boldsymbol{C}_1$ and $\boldsymbol{C}_2$ can be extracted from the matrices$\boldsymbol{DR}-\boldsymbol{H}$,$\boldsymbol{G}$,$\boldsymbol{C}$. The specific form can be expressed as.

$$\begin{bmatrix}(\boldsymbol{DR}-\boldsymbol{H})_1\\(\boldsymbol{DR}-\boldsymbol{H})_2\end{bmatrix}=\begin{bmatrix}(\boldsymbol{DR}-\boldsymbol{H})_{(N_{b1}\times N_{b1})}\\(\boldsymbol{DR}-\boldsymbol{H})_{(N_u\times N_{b1})}\end{bmatrix} \tag{16}$$

$$\begin{bmatrix}\boldsymbol{G}_1\\\boldsymbol{G}_2\end{bmatrix}=\begin{bmatrix}\boldsymbol{G}_{(N_{b1}\times N_{b2})}\\\boldsymbol{G}_{(N_u\times N_{b2})}\end{bmatrix} \tag{17}$$

$$\begin{bmatrix}\boldsymbol{C}_1\\\boldsymbol{C}_2\end{bmatrix}=\begin{bmatrix}\boldsymbol{C}_{(N_{b1}\times N_t)}\\\boldsymbol{C}_{(N_u\times N_t)}\end{bmatrix} \tag{18}$$

Substituting Eqs. (11)–(14) into Eq. (10), the ordinary differential system can be rewritten as.

$$\begin{bmatrix}\widetilde{\boldsymbol{\psi}}_{11} & \widetilde{\boldsymbol{\psi}}_{12}\\\widetilde{\boldsymbol{\psi}}_{21} & \widetilde{\boldsymbol{\psi}}_{22}\end{bmatrix}\begin{bmatrix}\dot{\widetilde{\boldsymbol{T}}}_{b1}\\\dot{\widetilde{\boldsymbol{T}}}_u\end{bmatrix}=\begin{bmatrix}\breve{\boldsymbol{\psi}}_{11} & \breve{\boldsymbol{\psi}}_{12}\\\breve{\boldsymbol{\psi}}_{21} & \breve{\boldsymbol{\psi}}_{22}\end{bmatrix}\begin{bmatrix}\boldsymbol{q}_{b1}\\\widetilde{\boldsymbol{T}}_u\end{bmatrix}+\begin{bmatrix}\widehat{\boldsymbol{\psi}}_1\\\widehat{\boldsymbol{\psi}}_2\end{bmatrix} \tag{19}$$

The unknown HFECCP $\boldsymbol{q}_{b1}$ in Eq. (19) can be expressed as.

$$\boldsymbol{q}_{b1}=\breve{\boldsymbol{\Psi}}_{11}^{-1}\left(\widetilde{\boldsymbol{\Psi}}_{11}\dot{\widetilde{\boldsymbol{T}}}_{b1}+\widetilde{\boldsymbol{\Psi}}_{12}\dot{\widetilde{\boldsymbol{T}}}_u-\breve{\boldsymbol{\Psi}}_{12}\widetilde{\boldsymbol{T}}_u-\widehat{\boldsymbol{\Psi}}_1\right) \tag{20}$$

Substituting Eq. (20) into Eq. (19), the ODEs with unknown normalized temperature only can be obtained as follows.

$$\dot{\widetilde{\boldsymbol{T}}}_u(t)=\boldsymbol{B}\widetilde{\boldsymbol{T}}_u(t)+\boldsymbol{F}_u(t) \tag{21}$$

where.

$$\boldsymbol{B}=\boldsymbol{C}_3(\breve{\boldsymbol{\Psi}}_{22}-\boldsymbol{C}_5\breve{\boldsymbol{\Psi}}_{12}) \tag{22}$$

$$\begin{aligned}\boldsymbol{F}_u(t)=\boldsymbol{C}_3\Big\{&\boldsymbol{C}_4\dot{\widetilde{\boldsymbol{T}}}_{b1}(t)+\left[(\boldsymbol{DR}-\boldsymbol{H})_2-\boldsymbol{C}_5(\boldsymbol{DR}-\boldsymbol{H})_1\right]\widetilde{\boldsymbol{T}}_{b1}(t)+\\&(\boldsymbol{G}_2-\boldsymbol{C}_5\boldsymbol{G}_1)\boldsymbol{q}_{b2}(t)+(\boldsymbol{C}_2-\boldsymbol{C}_5\boldsymbol{C}_1)\boldsymbol{g}(t)\Big\}\end{aligned} \tag{23}$$

in which.

$$\begin{cases}\boldsymbol{C}_3=(\widetilde{\boldsymbol{\Psi}}_{22}-\boldsymbol{C}_5\widetilde{\boldsymbol{\Psi}}_{12})^{-1}\\\boldsymbol{C}_4=\boldsymbol{C}_5\widetilde{\boldsymbol{\Psi}}_{11}-\widetilde{\boldsymbol{\Psi}}_{21}\\\boldsymbol{C}_5=\breve{\boldsymbol{\Psi}}_{21}\breve{\boldsymbol{\Psi}}_{11}^{-1}\end{cases} \tag{24}$$

3.2. Precise integration method

To facilitate the performance of IG-DRBEM to solve the transient heat transfer problem, the PIM is adopted to solve Eq. (21). For the s-th time step$[t_s,t_{s+1}]$, the solution is analytically written as.

$$\widetilde{\boldsymbol{T}}_u(t_{s+1})=\widehat{\boldsymbol{E}}\widetilde{\boldsymbol{T}}_u(t_s)+\int_0^{\Delta t_s}\exp[\boldsymbol{B}(\Delta t_s-\tau)]\boldsymbol{F}_u(t_s+\tau)\mathrm{d}\tau \tag{25}$$

where $\Delta t_s=t_{s+1}-t_s$ is the s-th time step. In this paper, the constant time step is carried out, i.e.$\Delta t_s=\Delta t$.

$\widehat{\boldsymbol{E}}$ in Eq. (25) is an exponential matrix, that is,$\widehat{\boldsymbol{E}}=\exp(\boldsymbol{B}\Delta t)$. How to calculate the matrix $\widehat{\boldsymbol{E}}$ accurately is the most important part of the PIM. The matrix $\widehat{\boldsymbol{E}}$ can be rewritten as.

$$\widehat{\boldsymbol{E}}=[\exp(\boldsymbol{B}\Delta t/\widetilde{m})]^{\widetilde{m}} \tag{26}$$

where $\widetilde{m}$ is an integer. Let$\widetilde{m} = 2^M$, where M is an integer. To improve the computational efficiency, the adaptive selection scheme of M is adopted. The detailed introduction can be seen in the literature [56,57]. The detailed derivation of calculation matrix $\widehat{\boldsymbol{E}}$ is shown in Eqs. (60)–(65) in the literature [37].

How to accurately carry out the integral operation in Eq. (25) is related to the accuracy of the final result$\widetilde{\boldsymbol{T}}_u$. $\boldsymbol{F}_u$ in Eq. (25) is formed by the known temperature and heat flux boundary conditions or heat sources. When the integral $\int_0^{\Delta t}(\cdot)\,\mathrm{d}\tau$ can be integrated analytically, the numerical results are not limited by the time step. If the integral $\int_0^{\Delta t}(\cdot)\,\mathrm{d}\tau$ is too complicated to integrate analytically, $\boldsymbol{F}_u$ can be approximated by the constant, linear or quadratic function. For example, use constant function to approximate $\boldsymbol{F}_u(t_s+\tau)$ i.e.$\boldsymbol{F}_u(t_s+\tau) = \boldsymbol{F}_u(t_{s+1})$. Finally, the unknown $\widetilde{\boldsymbol{T}}_u$ in Eq. (25) can be obtained as follows.

$$\widetilde{\boldsymbol{T}}_u(t_{s+1}) = \widehat{\boldsymbol{E}}\widetilde{\boldsymbol{T}}_u(t_s) + \boldsymbol{A}\boldsymbol{F}_u(t_{s+1}) \tag{27}$$

where.

$$\boldsymbol{A} = \widehat{\boldsymbol{E}}\boldsymbol{B}^{-1} - \boldsymbol{B}^{-1} \tag{28}$$

After the unknown $\widetilde{\boldsymbol{T}}_u$ is obtained, the unknown HFECCP can be calculated by Eq. (20). When the unknown NTECCP ($\boldsymbol{T}_{b2}$) and HFECCP ($\boldsymbol{q}_{b1}$) are solved, the normalized temperature and heat flux of boundary collocation points can be calculated by NURBS interpolation on the corresponding element. Finally, the real temperature of boundary collocation points and interior points can be solved by$T(\boldsymbol{x},\ t) = \widetilde{T}(\boldsymbol{x})/k(\boldsymbol{x})$.

3.3. Calculation of any interior and boundary points

When using NURBS to describe geometric information, the IGBEM needs only a few elements to accurately describe the boundary of the model. Naturally, the IGBEM can only directly obtain the result of a few boundary collocation points. It is very necessary to solve the response at any point on the boundary, so we first determined the element to which the point belongs, and then uses NURBS interpolation to solve the problem. To solve the temperature of any point in the domain, the obtained boundary information is used to generate the corresponding matrix, similar to the traditional BEM. A detailed description of these post-processing steps can be seen in reference [36].

4. Inversion of boundary conditions

4.1. Inversion of heat flux boundary conditions

It is well known that specifying the information of measurement points is necessary to solve the inverse problem. In this paper, the calculated normalized temperature of partial boundary collocation points is used as measurement information. Exploring the relationship between the information of measurement points and the quantity to be inversed is the most important step to establish the theory of non-iterative inversion. In this part, assume that the heat flux on the boundary Γ_2 needs to be identified. Before identifying the heat flux, the relationship between the normalized temperature of measurement points and the unknown $\boldsymbol{q}_{b2}$ should be explored. By integrating Eq. (27), the relationship between $\widetilde{\boldsymbol{T}}_u$ and $\boldsymbol{q}_{b2}$ can be obtained as follows.

$$\widetilde{\boldsymbol{T}}_u(t_{s+1}) = \boldsymbol{B}_u\boldsymbol{q}_{b2}(t_{s+1}) + \boldsymbol{b}(t_{s+1}) \tag{29}$$

where.

$$\boldsymbol{B}_u = \boldsymbol{A}\boldsymbol{C}_3(\boldsymbol{G}_2 - \boldsymbol{C}_5\boldsymbol{G}_1) \tag{30}$$

$$\begin{aligned}\boldsymbol{b}(t_{s+1}) = \widehat{\boldsymbol{E}}\widetilde{\boldsymbol{T}}_u(t_s) + \boldsymbol{A}\boldsymbol{C}_3\Big\{&\big[(\boldsymbol{D}\boldsymbol{R}-\boldsymbol{H})_2 - \boldsymbol{C}_5(\boldsymbol{D}\boldsymbol{R}-\boldsymbol{H})_1\big]\widetilde{\boldsymbol{T}}_{b1}(t_{s+1}) \\ &+ \boldsymbol{C}_4\dot{\widetilde{\boldsymbol{T}}}_{b1}(t_{s+1}) + (\boldsymbol{C}_2 - \boldsymbol{C}_5\boldsymbol{C}_1)\boldsymbol{g}(t_{s+1})\Big\}\end{aligned} \tag{31}$$

Therefore, the relationship between the normalized temperature of measurement point $\widetilde{\boldsymbol{T}}_{ue}$ and $\boldsymbol{q}_{b2}$ can be extracted from Eq. (29), i.e.

$$\widetilde{\boldsymbol{T}}_{ue}(t_{s+1}) = \boldsymbol{B}_{ue}\boldsymbol{q}_{b2}(t_{s+1}) + \boldsymbol{b}_e(t_{s+1}) \tag{32}$$

Further clarification is required that the matrix $\boldsymbol{B}_{ue}$ and the vector $\boldsymbol{b}_e$ are taken from the matrix $\boldsymbol{B}_u = [\boldsymbol{B}_{u1};\boldsymbol{B}_{ue}]$ and$\boldsymbol{b}(t_{s+1}) = \{\boldsymbol{b}_1(t_{s+1});\boldsymbol{b}_e(t_{s+1})\}$, respectively. Here, it needs to be clarified again that the boundary quantities $\widetilde{\boldsymbol{T}}_{ue}$ and $\boldsymbol{q}_{b2}$ in Eq. (32) correspond to the control point expansion coefficients. In the process of solving the inverse problem, the real normalization temperature $\widetilde{\boldsymbol{T}}^r_{ue}$ of the collocation points is required. Based on Eq. (32), $\widetilde{\boldsymbol{T}}^r_{ue}$ can be given by.

$$\widetilde{T}^r_{ue}(t_{s+1}) = B^r_{ue}q_{b2}(t_{s+1}) + b^r_e(t_{s+1}) \tag{33}$$

where $\widetilde{T}^r_{ue} = R^r_{ue}\widetilde{T}_{ue}$, $B^r_{ue} = R^r_{ue}B_{ue}$, $b^r_e = R^r_{ue}b_e$, and R^r_{ue} is generated by the NURBS shape function corresponding to the collocation point.

Then, the error function $\boldsymbol{J}$ is established as follows.

$$J = \left\|\widetilde{\boldsymbol{T}}^r_{ue}(t_{s+1}) - \widetilde{\boldsymbol{T}}^r_{um}(t_{s+1})\right\|_2^2 \tag{34}$$

where the superscript “T” denotes the transpose of the vector, $\widetilde{\boldsymbol{T}}^r_{um}$ is the normalized temperature of measurement points. Generally, $\widetilde{\boldsymbol{T}}^r_{um}$ is obtained by the numerical simulation or the experimental operation. In this paper, $\widetilde{\boldsymbol{T}}^r_{um}$ calculated by IG-DRBEM is utilized to replace the measured value.

To find the optimal$\boldsymbol{q}_{b2}$, $\boldsymbol{J}$ can be minimized by differentiating $\boldsymbol{J}$ with respect to $\boldsymbol{q}_{b2}$ as follows.

$$\partial J/\partial \boldsymbol{q}_{b2} = 0 \tag{35}$$

So, $\boldsymbol{q}_{b2}$ can be written as.

$$\boldsymbol{q}_{b2}(t_{s+1}) = \left(\left(\boldsymbol{B}^r_{ue}\right)^{\mathrm{T}}\boldsymbol{B}^r_{ue}\right)^{-1}\left(\boldsymbol{B}^r_{ue}\right)^{\mathrm{T}}\left[\widetilde{\boldsymbol{T}}^r_{um}(t_{s+1}) - \boldsymbol{b}^r_e(t_{s+1})\right] \tag{36}$$

In general, $\left(\boldsymbol{B}^r_{ue}\right)^{\mathrm{T}}\boldsymbol{B}^r_{ue}$ is an ill-conditioned matrix. The truncated singular value decomposition (TSVD) method is adopted to implement matrix inversion. When the HFECCPs are obtained, the unknown heat flux of collocation points can be solved by NURBS interpolation.

In order to improve the performance of the present inversion scheme, the basis function expansion method is adopted. The HFECCP to be inversed is expanded by using basis functions. Here, a set of complete polynomials independent of time is used as expanding basis functions. It is worth noting that the representation of the collocation point heat flux needs to be multiplied by a transformation matrix $\boldsymbol{R}$ in front of the HFECCP$\boldsymbol{q}_{b2}$. For instance, the $\boldsymbol{q}_{b2}$ can be expressed as.

$$\boldsymbol{R}_{i,N_{b2}}\boldsymbol{q}_{b2}(t_{s+1}) = \sum_{j=1}^{\widetilde{k}}\alpha_j(t_{s+1})\phi_j\left(x_{1,i},x_{2,i},x_{3,i}\right) \tag{37}$$

where $\boldsymbol{R}_{i,N_{b2}}$ is extracted from the matrix $\boldsymbol{R}$ in Eq. (7), the basis function $\phi_j, (j = 1,2,\cdots,\widetilde{k})$ is given by.

$$\{\phi_1,\phi_2,\cdots,\phi_{\widetilde{k}}\} = \begin{cases} \widetilde{\phi}_1 = \{1,x_1,x_2,x_3\}, & \widetilde{k} = 4 \\ \widetilde{\phi}_2 = \widetilde{\phi}_1 \cup \{x_1^2,x_2^2,x_3^2,x_1x_2,x_1x_3,x_2x_3\}, & \widetilde{k} = 10 \\ \widetilde{\phi}_3 = \widetilde{\phi}_2 \cup \{x_1^3,x_2^3,x_3^3,x_1x_2x_3,x_1^2x_2,x_1^2x_3, & \\ x_2^2x_1,x_2^2x_3,x_3^2x_1,x_3^2x_2\}, & \widetilde{k} = 20 \end{cases} \tag{38}$$

It can be seen that the number of basis functions in linear, quadratic and cubic polynomials is 4, 10 and 20, respectively. Applying Eq. (37) to each collocation point of the heat flux to be inversed, the matrix form using quadratic basis functions can be obtained as follows.

$$\boldsymbol{R}_{(N_{b2}\times N_{b2})}\boldsymbol{q}_{b2}(t_{s+1}) = \boldsymbol{\Phi}\boldsymbol{\alpha}(t_{s+1}) \tag{39}$$

where.

$$\boldsymbol{\Phi}=\begin{bmatrix}1 & x_{1,1} & x_{2,1} & \cdots & x_{2,1}x_{3,1}\\ 1 & x_{1,2} & x_{2,2} & \cdots & x_{2,2}x_{3,2}\\ \vdots & \vdots & \vdots & \vdots & \vdots\\ 1 & x_{1,N_{b2}} & x_{2,N_{b2}} & \cdots & x_{2,N_{b2}}x_{3,N_{b2}}\end{bmatrix}_{(N_{b2}\times 10)} \tag{40}$$

$$\boldsymbol{\alpha}(t_{s+1})=\{\alpha_1(t_{s+1}),\alpha_2(t_{s+1}),\cdots,\alpha_{10}(t_{s+1})\}^{\mathrm{T}} \tag{41}$$

According to the formula (39), $\boldsymbol{q}_{b2}(t_{s+1})$ can be rewritten as.

$$\boldsymbol{q}_{b2}(t_{s+1})=\boldsymbol{R}^{-1}_{(N_{b2}\times N_{b2})}\boldsymbol{\Phi}\boldsymbol{\alpha}(t_{s+1}) \tag{42}$$

Note that the transformation matrix $\boldsymbol{\Phi}$ only needs to be evaluated once because the expansion basis function only depends on the spatial coordinates.

Substituting Eq. (42) into Eq. (33), a new relationship between $\widetilde{\boldsymbol{T}}^{r}_{ue}$ and $\boldsymbol{q}_{b2}$ can be expressed as.

$$\widetilde{\boldsymbol{T}}^{r}_{ue}(t_{s+1})=\widehat{\boldsymbol{D}}\boldsymbol{\alpha}(t_{s+1})+\boldsymbol{b}^{r}_{e}(t_{s+1}) \tag{43}$$

where$\widehat{\boldsymbol{D}}=\boldsymbol{B}^{r}_{ue}\boldsymbol{R}^{-1}_{(N_{b2}\times N_{b2})}\boldsymbol{\Phi}$. Similar to Eq. (35), by executing$\partial J/\partial\boldsymbol{\alpha}(t_{s+1})=0$, the optimal $\boldsymbol{\alpha}(t_{s+1})$ can be obtained as follows.

$$\boldsymbol{\alpha}(t_{s+1})=\left(\widehat{\boldsymbol{D}}^{\mathrm{T}}\widehat{\boldsymbol{D}}\right)^{-1}\widehat{\boldsymbol{D}}^{\mathrm{T}}\left[\widetilde{\boldsymbol{T}}^{r}_{um}(t_{s+1})-\boldsymbol{b}^{r}_{e}(t_{s+1})\right] \tag{44}$$

Finally, the heat flux of collocation points can be solved by the right-hand side of Eq. (39).

4.2. *Inversion of temperature boundary conditions*

Assuming that the temperature on the boundary Γ_1 is unknown, this section mainly introduces the inversion of temperature boundary conditions, which is similar to the inversion of heat flux boundary conditions. Before inversing boundary unknown temperature, based on the Eq. (27) the relationship between the real normalization temperature of the measuring point and the NTECCP to be inversed should be explored. Firstly, Eq. (27) can be rewritten as.

$$\widetilde{\boldsymbol{T}}_{u}(t_{s+1})=\widetilde{\boldsymbol{B}}_{u}\widetilde{\boldsymbol{T}}_{b1}(t_{s+1})+\widetilde{\boldsymbol{b}}(t_{s+1}) \tag{45}$$

where.

$$\widetilde{\boldsymbol{B}}_{u}=\boldsymbol{A}\boldsymbol{C}_3\left[\frac{\boldsymbol{C}_4}{\Delta t}+(\boldsymbol{D}\boldsymbol{R}-\boldsymbol{H})_2-\boldsymbol{C}_5(\boldsymbol{D}\boldsymbol{R}-\boldsymbol{H})_1\right] \tag{46}$$

$$\begin{aligned}\widetilde{\boldsymbol{b}}(t_{s+1})=\widehat{\boldsymbol{E}}\widetilde{\boldsymbol{T}}_{u}(t_s)+\boldsymbol{A}\boldsymbol{C}_3\Big[&(\boldsymbol{G}_2-\boldsymbol{C}_5\boldsymbol{G}_1)\boldsymbol{q}_{b2}(t_{s+1})\\ &-\frac{\boldsymbol{C}_4}{\Delta t}\widetilde{\boldsymbol{T}}_{b1}(t_s)+(\boldsymbol{C}_2-\boldsymbol{C}_5\boldsymbol{C}_1)\boldsymbol{g}(t_{s+1})\Big]\end{aligned} \tag{47}$$

Similar to the process from Eq. (32) to Eq. (44), the normalized temperature coefficients of measuring points $\widetilde{\boldsymbol{T}}_{ue}$ can be extracted from Eq. (45) in the following form.

$$\widetilde{\boldsymbol{T}}_{ue}(t_{s+1})=\widetilde{\boldsymbol{B}}_{ue}\widetilde{\boldsymbol{T}}_{b1}(t_{s+1})+\widetilde{\boldsymbol{b}}_{e}(t_{s+1}) \tag{48}$$

where the matrix $\widetilde{\boldsymbol{B}}_{ue}$ and the vector $\widetilde{\boldsymbol{b}}_{e}$ are taken from the matrix $\widetilde{\boldsymbol{B}}_{u}=[\widetilde{\boldsymbol{B}}_{u1};\widetilde{\boldsymbol{B}}_{ue}]$ and$\widetilde{\boldsymbol{b}}(t_{s+1})=\{\widetilde{\boldsymbol{b}}_{1}(t_{s+1});\widetilde{\boldsymbol{b}}_{e}(t_{s+1})\}$, respectively.

Similar to Eq. (33), the relationship of real normalization temperatures $\widetilde{\boldsymbol{T}}^{r}_{ue}$ and $\widetilde{\boldsymbol{T}}_{b1}$ can be given by.

$$\widetilde{\boldsymbol{T}}^{r}_{ue}(t_{s+1})=\widetilde{\boldsymbol{B}}^{r}_{ue}\widetilde{\boldsymbol{T}}_{b1}(t_{s+1})+\widetilde{\boldsymbol{b}}^{r}_{e}(t_{s+1}) \tag{49}$$

where$\widetilde{\boldsymbol{T}}^{r}_{ue}=\widetilde{\boldsymbol{R}}^{r}_{ue}\widetilde{\boldsymbol{T}}_{ue}$, $\widetilde{\boldsymbol{B}}^{r}_{ue}=\widetilde{\boldsymbol{R}}^{r}_{ue}\widetilde{\boldsymbol{B}}_{ue}$,$\widetilde{\boldsymbol{b}}^{r}_{e}=\widetilde{\boldsymbol{R}}^{r}_{ue}\widetilde{\boldsymbol{b}}_{e}$, and $\widetilde{\boldsymbol{R}}^{r}_{ue}$ is generated by the NURBS shape function corresponding to the collocation point. The basis function is used to expand the normalized temperature of collocation points, i.e.

$$\boldsymbol{R}_{(N_{b1}\times N_{b1})}\widetilde{\boldsymbol{T}}_{b1}(t_{s+1})=\boldsymbol{\Phi}\boldsymbol{\alpha}(t_{s+1}) \tag{50}$$

Then, the optimal $\boldsymbol{\alpha}(t_{s+1})$ can be obtained by solving $\partial J/\partial\boldsymbol{\alpha}(t_{s+1})=0$ in the following form.

$$\boldsymbol{\alpha}(t_{s+1})=\left(\breve{\boldsymbol{D}}^{\mathrm{T}}\breve{\boldsymbol{D}}\right)^{-1}\breve{\boldsymbol{D}}^{\mathrm{T}}\left[\widetilde{\boldsymbol{T}}^{r}_{um}(t_{s+1})-\widetilde{\boldsymbol{b}}^{r}_{e}(t_{s+1})\right] \tag{51}$$

where$\breve{\boldsymbol{D}}=\widetilde{\boldsymbol{B}}^{r}_{ue}\boldsymbol{R}^{-1}_{(N_{b1}\times N_{b1})}\boldsymbol{\Phi}$. Finally, the unknown temperature of collocation points can be calculated from the term on the right of Eq. (50).

The detailed flowchart of solving the forward and inverse problem is shown in Fig. 2.

5. Numerical examples

In order to show the performance of the presented approach, the absolute error (Abserr), the relative error (Relerr) and the relative L_2 error norm (e_{L_2}) are used. These errors are given by.

$$\begin{cases}\text{Abserr} = \left|\gamma_{com}-\gamma_{ref}\right|\\ \text{Relerr} = 100\cdot\left|\gamma_{com}-\gamma_{ref}\right|/\left|\gamma_{ref}\right|\\ e_{L_2}=\left\|\gamma_{com}-\gamma_{ref}\right\|_{L_2}/\left\|\gamma_{ref}\right\|_{L_2}\end{cases} \tag{52}$$

where the L_2 norm $\left\|\gamma_{ref}\right\|_{L_2}$ is written as follows.

$$\left\|\gamma_{ref}\right\|_{L_2}=\sqrt{\sum_{i=1}^{N_t}\gamma^2_{ref,i}} \tag{53}$$

In addition, the maximum Abserr (Mabserr) and the maximum Relerr (Mrelerr) are also adopted to judge the performance of the proposed method. The subscripts “*com*” and “*ref*” in Eqs. (52) and (53) represent the computed numerical result and the reference solution of temperature or heat flux. For the convenience of subsequent expression, the total number of patches, elements and control points is represented byN_p, N_e andN_c, respectively.

5.1. *A cube model*

In this example, a cube of length, width and height $2\times2\times2$ is considered. As shown in Fig. 3, the initial model is divided into 6 elements in total, in which each surface of the cube is distributed with a NURBS element and each element includes 9 collocation points. At the same time, the 53 interior points are uniformly distributed within the domain.

To verify the effectiveness of the proposed method, the analytical expression of the temperature field is assumed as.

$$T=(x_1+3x_2+5x_3+10)\cos(50t) \tag{54}$$

where the physical parameters$k(\boldsymbol{x})$,$\rho(\boldsymbol{x})$, $c(\boldsymbol{x})$ and the heat source $g(\boldsymbol{x})$ are given by.

$$\begin{cases}k=e^{x_1+x_2}\quad;\quad \rho=x_1+5\quad;\quad c=\cos(x_1x_2x_3)\\ g=-50\rho c(x_1+3x_2+5x_3+10)\sin(50t)-4e^{x_1+x_2}\cos(50t)\end{cases} \tag{55}$$

In this example, the temperature boundary condition is specified by Eq. (54). To accurately solve the integral $\int_0^{\Delta t_s}(\cdot)\,\mathrm{d}\tau$ in Eq. (25), based on the expression of the temperature boundary condition and heat source function, $\boldsymbol{F}_u$ can be written as.

$$\boldsymbol{F}_u(t)=\boldsymbol{F}_1\cos(50t)+\boldsymbol{F}_2 sin(50t) \tag{56}$$

Thus, based on the Eq. (25), $\widetilde{\boldsymbol{T}}_u$ can be expressed as.

$$\begin{aligned}\widetilde{\boldsymbol{T}}_u(t_{s+1}) = \widehat{\boldsymbol{E}}\widetilde{\boldsymbol{T}}_u(t_s) + \frac{1}{50}\Big[&\boldsymbol{I}\cdot sin(50t_{s+1}) - \frac{\boldsymbol{B}}{50}\cdot\cos(50t_{s+1}) \\ &- \widehat{\boldsymbol{E}}\cdot sin(50t_s) + \frac{\widehat{\boldsymbol{E}}\boldsymbol{B}}{50}\cdot\cos(50t_s)\Big]\cdot\left(\boldsymbol{I}+\frac{\boldsymbol{B}^2}{50^2}\right)^{-1}\cdot\boldsymbol{F}_1 \\ +\frac{1}{50}\Big[&\widehat{\boldsymbol{E}}\cdot\cos(50t_s) + \frac{\widehat{\boldsymbol{E}}\boldsymbol{B}}{50}\cdot\sin(50t_s) - \boldsymbol{I}\cdot\cos(50t_{s+1}) \\ &- \frac{\boldsymbol{B}}{50}\cdot\cos(50t_{s+1})\Big]\cdot\left(\boldsymbol{I}+\frac{\boldsymbol{B}^2}{50^2}\right)^{-1}\cdot\boldsymbol{F}_2\end{aligned} \tag{57}$$

where $\boldsymbol{I}$ is the identity matrix of the same order as$\boldsymbol{B}$.

(A) The effect of different β on the results.

As shown in Fig. 3, different shrinkage coefficients β result in different distributions of collocation points between patches. Here, the results of temperature at the $t_{end} = 1$ are presented, where $\Delta t = 1$ is adopted. It can be seen from Table 1 that β cannot be too big or too small. For instance, 0.3 is the optimal β by comparison. So, $\beta = 0.30$ is taken in the subsequent calculation.

(B) The effect of using single-patch and multi-patch modeling on the results.

To show the performance of the proposed collocation scheme for multi-patch modeling, the same cube is established by the single-patch and multi-patch technique. As shown in Fig. 4, different distribution schemes of collocation points are considered, where 53 interior points are used in each calculation model.

The results of different numbers of collocation points by progressively refinement at $t_{end} = 1$ are presented in Fig. 5 with$\Delta t = 1$. It can be seen that the multi-patch model can obtain higher accuracy than the single-patch model with fewer collocation points. However, if there are sufficient collocation points, the precision gap between the two configuration schemes will narrow.

(C) Different interpolation forms of$\boldsymbol{F}_u$.

When loads and heat source functions are too complex to separate time and space variables, that is, when $\int_0^{\Delta t_s}(\cdot)\,d\tau$ in Eq. (25) cannot be integrated analytically, it is necessary to consider interpolating $\boldsymbol{F}_u$ and then integrating it. To explore an effective approximation of$\boldsymbol{F}_u$, the constant, linear and quadratic approximations are discussed. Fig. 6 shows the e_{L_2} of the PIM calculation when $\boldsymbol{F}_u$ uses three kinds of approximations. For comparison, the results of using FDM to solve Eq. (7) are also presented in Fig. 6 at$t_{end} = 100$. It can be seen that when the time step is small, both PIM and FDM can obtain reliable accuracy, and the change of time step has almost no effect on the calculation accuracy of the PIM with analytical time term integration. Even in the case of the large time step, the quadratic approximation can still obtain a good agreement with analytic integration and is better than FDM. To show the applicability of PIM to arbitrary boundary conditions and heat sources under the premise of ensuring accuracy, the quadratic approximation $\boldsymbol{F}_u$ with $\Delta t = 0.01$ is utilized in the subsequent examples.

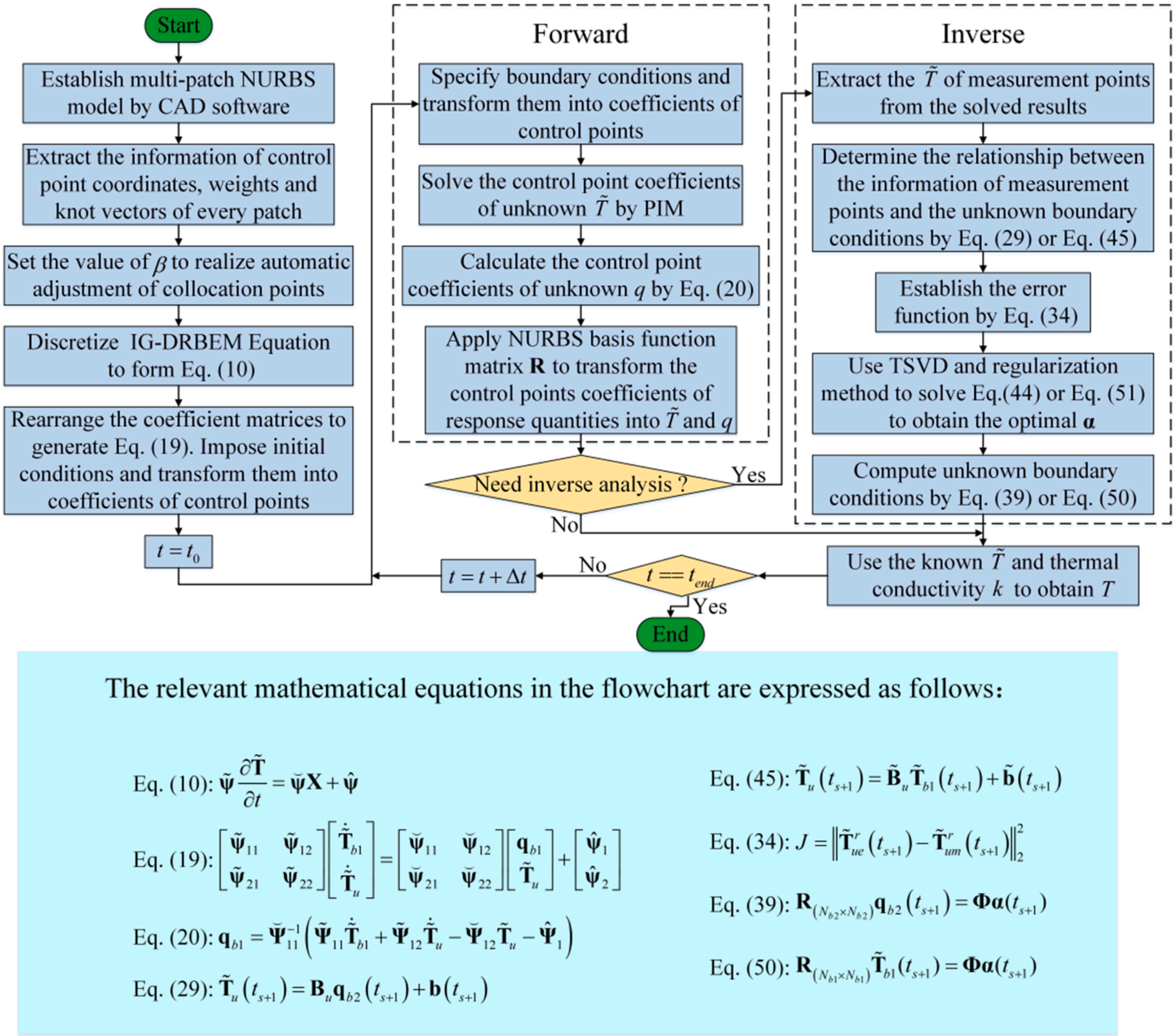

The relevant mathematical equations in the flowchart are expressed as follows:

Eq. (10): $\tilde{\boldsymbol{\psi}}\dfrac{\partial\tilde{\mathbf{T}}}{\partial t} = \breve{\boldsymbol{\psi}}\mathbf{X} + \hat{\boldsymbol{\psi}}$

Eq. (19): $\begin{bmatrix}\tilde{\boldsymbol{\Psi}}_{11} & \tilde{\boldsymbol{\Psi}}_{12}\\ \tilde{\boldsymbol{\Psi}}_{21} & \tilde{\boldsymbol{\Psi}}_{22}\end{bmatrix}\begin{bmatrix}\dot{\tilde{\mathbf{T}}}_{b1}\\ \dot{\tilde{\mathbf{T}}}_{u}\end{bmatrix} = \begin{bmatrix}\breve{\boldsymbol{\Psi}}_{11} & \breve{\boldsymbol{\Psi}}_{12}\\ \breve{\boldsymbol{\Psi}}_{21} & \breve{\boldsymbol{\Psi}}_{22}\end{bmatrix}\begin{bmatrix}\mathbf{q}_{b1}\\ \tilde{\mathbf{T}}_{u}\end{bmatrix} + \begin{bmatrix}\hat{\boldsymbol{\Psi}}_{1}\\ \hat{\boldsymbol{\Psi}}_{2}\end{bmatrix}$

Eq. (20): $\mathbf{q}_{b1} = \breve{\boldsymbol{\Psi}}_{11}^{-1}\left(\tilde{\boldsymbol{\Psi}}_{11}\dot{\tilde{\mathbf{T}}}_{b1} + \tilde{\boldsymbol{\Psi}}_{12}\dot{\tilde{\mathbf{T}}}_{u} - \breve{\boldsymbol{\Psi}}_{12}\tilde{\mathbf{T}}_{u} - \hat{\boldsymbol{\Psi}}_{1}\right)$

Eq. (29): $\tilde{\mathbf{T}}_u\left(t_{s+1}\right) = \mathbf{B}_u\mathbf{q}_{b2}\left(t_{s+1}\right) + \mathbf{b}\left(t_{s+1}\right)$

Eq. (45): $\tilde{\mathbf{T}}_u\left(t_{s+1}\right) = \tilde{\mathbf{B}}_u\tilde{\mathbf{T}}_{b1}\left(t_{s+1}\right) + \tilde{\mathbf{b}}\left(t_{s+1}\right)$

Eq. (34): $J = \left\|\tilde{\mathbf{T}}_{ue}^{r}\left(t_{s+1}\right) - \tilde{\mathbf{T}}_{um}^{r}\left(t_{s+1}\right)\right\|_2^2$

Eq. (39): $\mathbf{R}_{\left(N_{b2}\times N_{b2}\right)}\mathbf{q}_{b2}\left(t_{s+1}\right) = \boldsymbol{\Phi\alpha}(t_{s+1})$

Eq. (50): $\mathbf{R}_{\left(N_{b1}\times N_{b1}\right)}\tilde{\mathbf{T}}_{b1}(t_{s+1}) = \boldsymbol{\Phi\alpha}(t_{s+1})$

Fig. 2. The flowchart for solving the forward problem.and boundary condition inversion.

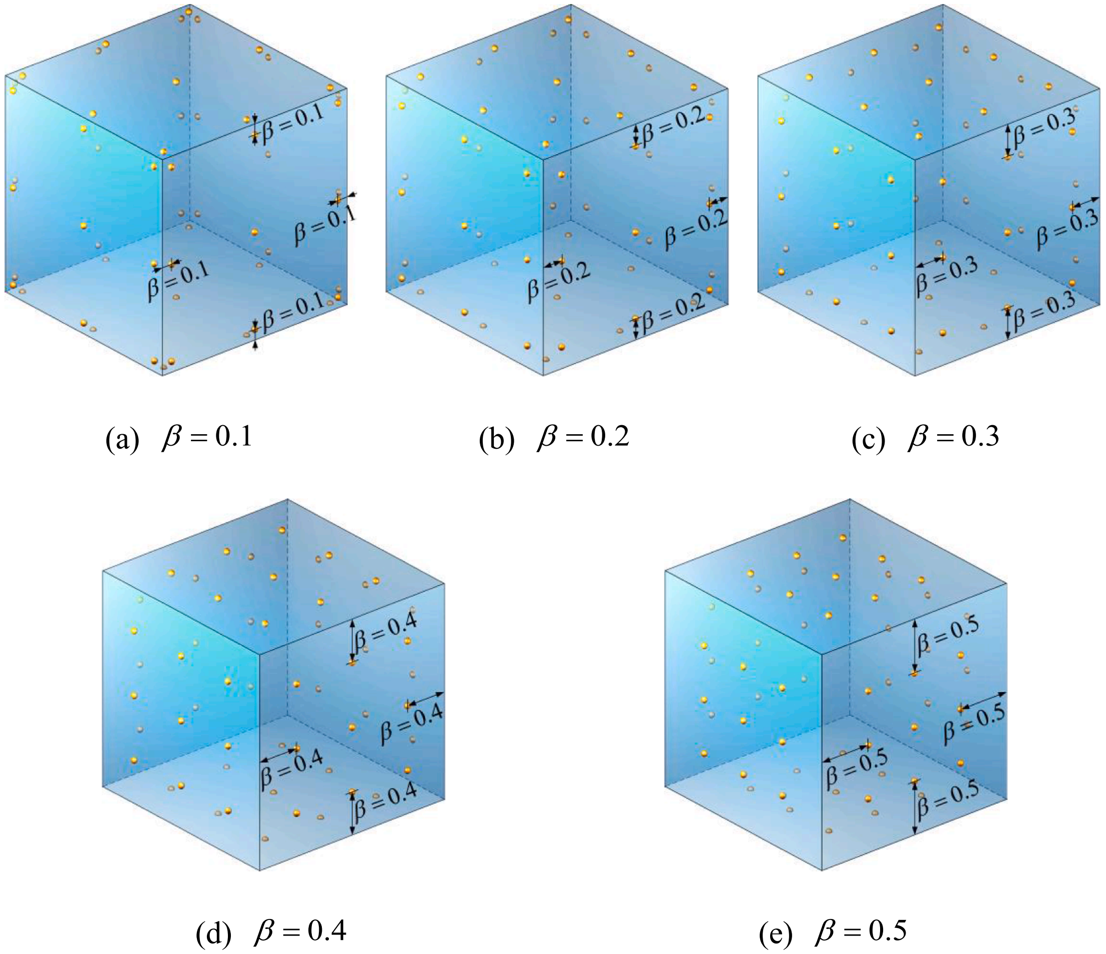

(a) $\beta = 0.1$ (b) $\beta = 0.2$ (c) $\beta = 0.3$

(d) $\beta = 0.4$ (e) $\beta = 0.5$

Fig. 3. IGBEM model of the cube with differentβ.

Table 1
Temperature errors for considering differentβ.

β	e_{L_2}	Mabserr	Mrelerr (%)
$\beta = 0.10$	4.7317e-4	0.0268	0.3008
$\beta = 0.20$	4.6401e-4	0.0284	0.2273
$\beta = 0.30$	2.3031e-4	0.0099	0.1071
$\beta = 0.40$	3.4724e-4	0.0206	0.2086
$\beta = 0.50$	7.5343e-4	0.0466	0.6358

5.2. A multi-patch sphere model

A sphere with radius 1 is established in this example to compare the present approach with the traditional BEM and test the effect of measuring point position on thermal load inversion results. The control points distribution and initial NURBS elements of the model are shown in Fig. 7.

To facilitate the verification of accuracy, assuming the temperature

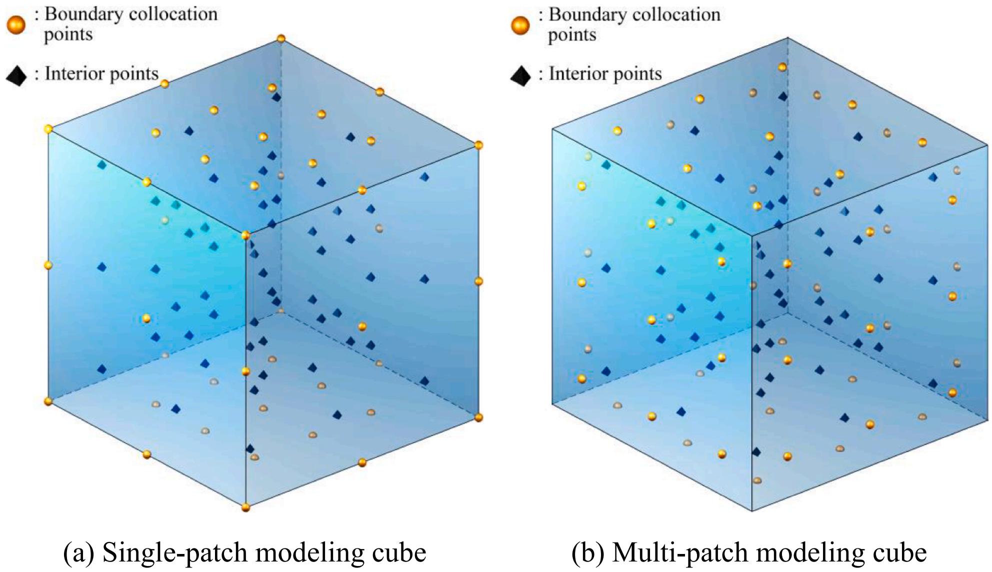

(a) Single-patch modeling cube (b) Multi-patch modeling cube

Fig. 4. Distribution of collocation points and interior points of the single-patch and multi-patch modeling cube.

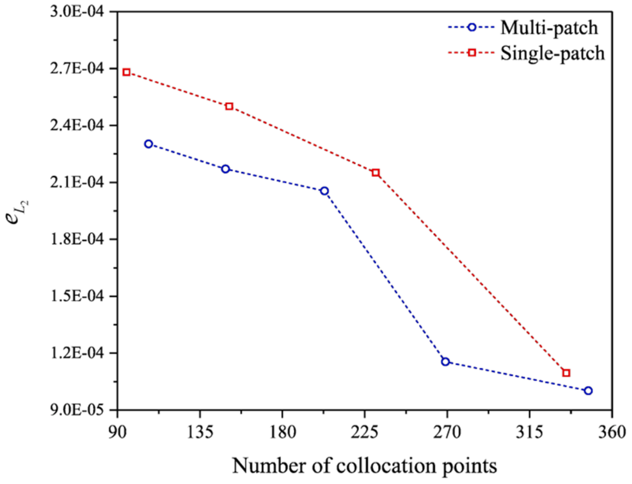

Fig. 5. Temperature e_{L_2} of considering different number of collocation points.

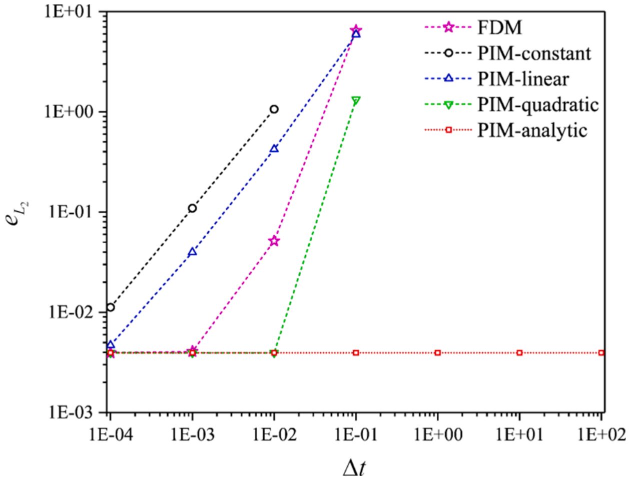

Fig. 6. Temperature results of using PIM and FDM with differentΔt.

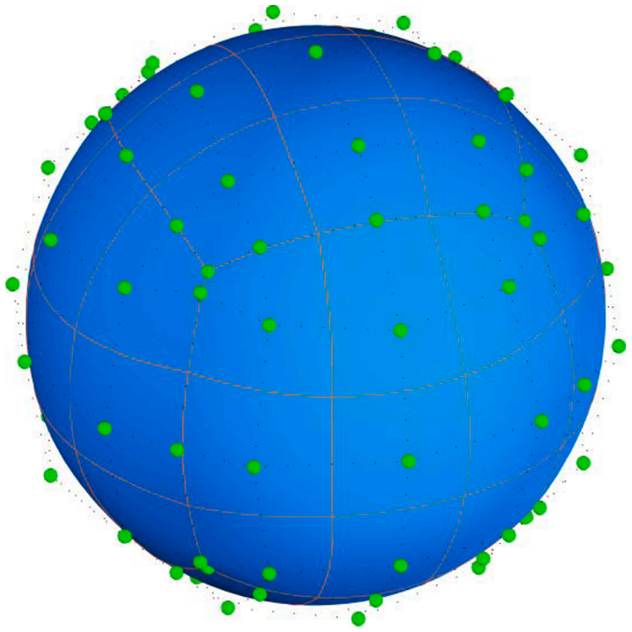

Fig. 7. The control points and the initial NURBS elements of the sphere.

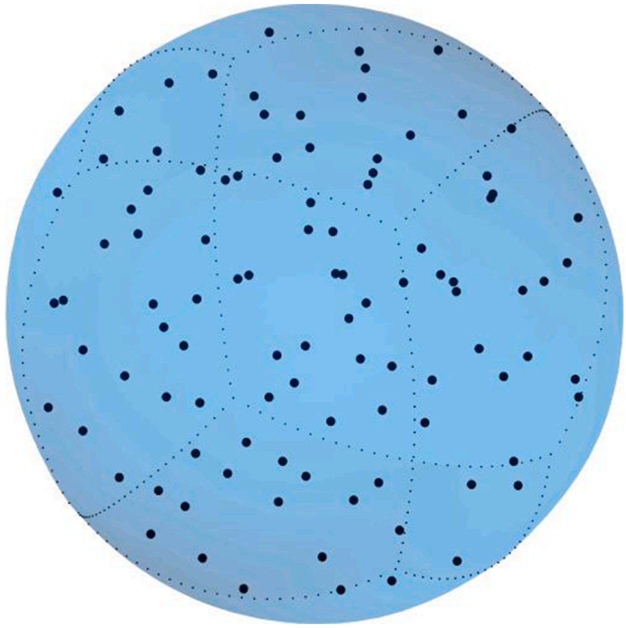

Fig. 8. The interior points distribution of case (A).

field of the sphere satisfies$T = 10\left[e^{x_1} + \cos(x_2) + x_3^2\right]e^t$. The pure temperature boundary condition and initial condition can be determined according to this equation, and the physical parameters and heat source of the model are given as follows:

$$\begin{cases} k = x_1^2 + x_2^2 + x_3^2 + 1 \quad ; \quad \rho = 1 \quad ; \quad c = 1 \\ g = 10e^t\left\{e^{x_1} + \cos(x_2) + x_3^2 - k\left[e^{x_1} - \cos(x_2) + 2\right] \right. \\ \left. \qquad - 2\left[x_1 e^{x_1} - x_2\sin(x_2) + 2x_3^2\right]\right\} \end{cases} \tag{58}$$

(A) Compare with traditional BEM.

This case computes the traditional BEM and multi-patch IG-DRBEM of gradually refined elements based on the 100 randomly distributed interior points shown in Fig. 8. Fig. 9 and Fig. 10 depict the different element discretization of the two methods, where the 8-node quadratic element is adopted in traditional BEM. Their temperature e_{L_2} at $t_{end} = 1$ corresponding to different degrees of freedom is described in Fig. 11. It can be obtained that the proposed method can achieve satisfactory precision higher than that of traditional BEM [58] when the degree of freedom is less, and the error levels of the two methods tend to be the same with enough degrees of freedom.

(B) The influence of measuring point positions.

Based on this simple sphere model, the influence of measuring point positions on temperature boundary condition identification is discussed here. The region of boundary conditions to be inversed and the adopted 75 interior points are shown in Fig. 12. The initial NURBS element in Fig. 9 (a) is used by the computational model. In order to highlight the differences between the positions of the measurement point, the interior points with $x_3 = 0.5,\ 0,\ -0.5$ in Fig. 12 are used as measuring points layer by layer.

It is evident from Table 2 that the inversion results are better when the distance between the measurement points and the boundary to be identified is small. In terms of this, the measurement points relatively close to the inversion boundary will be distributed in the subsequent thermal load identification procedure. In addition, the basis function expansion is not taken into account here because of the few variables to be inverted in this example.

5.3. A complex model of a fighter

In this example, inversion of temperature and heat flux boundary

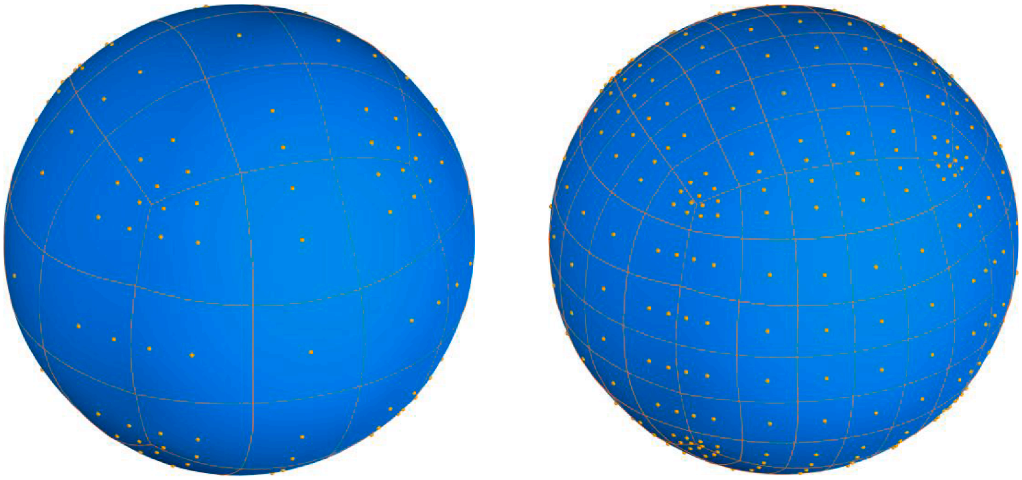

(a) 54 elements, 150 boundary collocation points

(b) 216 elements, 384 boundary collocation points

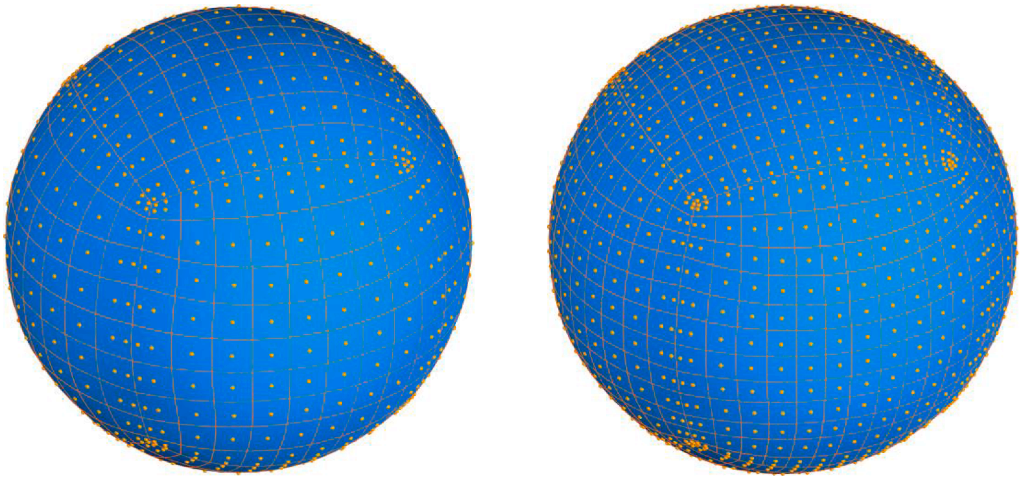

(c) 486 elements, 726 boundary collocation points

(d) 864 elements, 1176 boundary collocation points

Fig. 9. Different element divisions and boundary collocation points of IG-DRBEM.

conditions is investigated. As shown in Fig. 13, a complex NURBS model of fighter is used in the calculation process, where 500 points are distributed inside the fighter and represented by black dots. The model comes with two drop tanks and two simplified missile models, and the drop tank, cockpit and tail engine parts have been cut into proper cavity shapes. Table 3 provides the information of the computational model. The distribution of control points and NURBS elements and the region position of imposing boundary conditions are shown in Fig. 14, where on the outer surface of the upper part of the cockpit (OSUPC), the inner surface of the cavity of the cockpit part (ISCCP), the inner surface of the drop tank (ISDT), and the inner surface of the cavity of the engine part (ISCEP) are all subjected to heat flux boundary conditions, and the remaining parts are given temperature boundary conditions. In addition, in Fig. 14, the green dots denote the control point and the NURBS element is depicted by the blue line.

5.3.1. *The verification of forward problems*

The accuracy of the proposed method in solving complex models needs to be verified before boundary condition inversion. Here, it is assumed that the temperature field of the entire fighter is.

$$T = 10\left(\cos x_1 + x_2^2 + x_3 + 1\right)e^{-t} \tag{59}$$

where the thermal conductivity, density, specific heat capacity and heat source are given by.

$$\left\{\begin{array}{c} k = \ln(x_2+5);\rho = \cos\left(x_1^2\right);c = \cos(x_1x_2x_3) \\ g = -10e^{-t}\left[\cos\left(x_1^2\right)\cos(x_1x_2x_3)\left(\cos x_1 + x_2^2 + x_3 + 1\right)\right. \\ \left. +2x_2/(x_2+5) - \ln(x_2+5)(\cos x_1 - 2)\right] \end{array}\right. \tag{60}$$

It is worth noting that when the correctness of the forward problem is investigated, the assumed analytical temperature field expression Eq. (59) is directly used for conversion at the position where the heat flux boundary condition is applied to the fighter model, and the temperature boundary condition is directly applied by Eq. (59).

It can be seen from Table 4 that the presented method also has very stable and accurate performance for processing complex multi-patch geometric models, in which the maximum relative error is less than 0.035%. As shown in Fig. 15, the temperature error distributions at

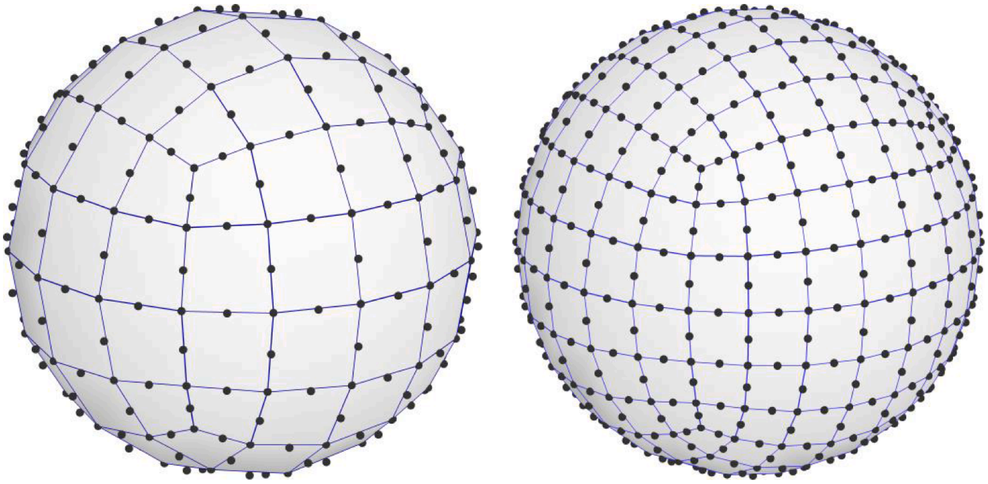

(a) 96 elements, 290 boundary nodes (b) 216 elements, 650 boundary nodes

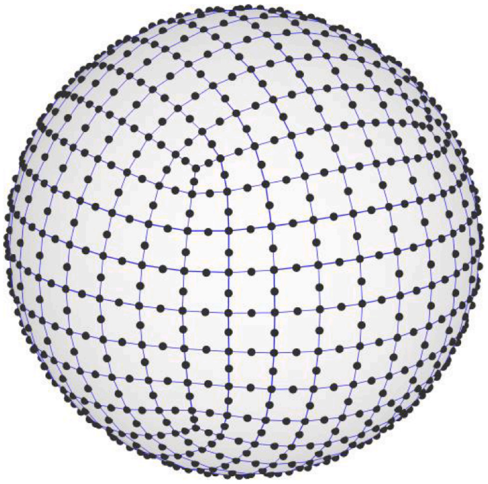

(c) 384 elements, 1154 boundary nodes

Fig. 10. Different element divisions and boundary nodes of conventional BEM.

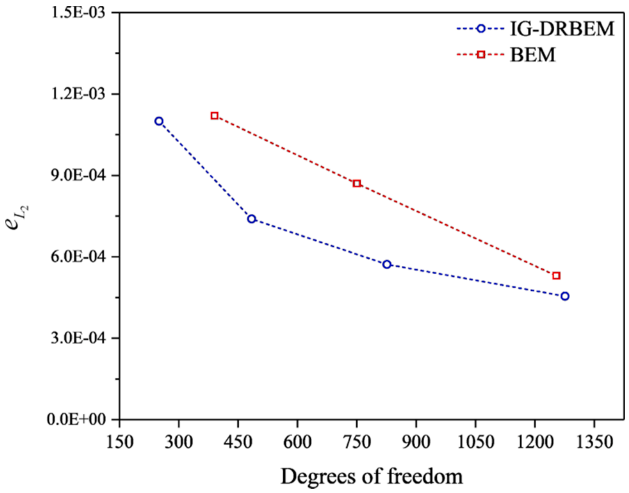

Fig. 11. Temperature e_{L_2} of different methods at $t_{end} = 1$.

different instants are relatively stable, and the Mrelerr distribution point is basically concentrated on the outer surface of the cockpit and the inner surface of the drop tank. However, the number of collocation points with large Relerrs is very small.

5.3.2. *The inversion of temperature boundary conditions*

In this case, it is assumed that the ISCCP, ISDT and ISCEP parts are adiabatic, at the same time, the OSUPC part is given a heat flux by.

$$q_{OSUPC} = 300(x_1 + x_2 + x_3 + 2)e^{-t} \tag{61}$$

and the rest part of the fighter is given a temperature boundary condition according to Eq. (59). Physical property parameters and heat source distribution are specified by Eq. (60). The temperature boundary conditions to be inversed are shown in Fig. 16, where the temperature of 552 collocation points needs to be inversed. In the inversion process, 104 measurement points are respectively distributed in ISCCP, ISDT and ISCEP positions, where the detailed distribution of measurement points can be seen in Fig. 17(b).

(A) The effect of different expansion basis functions.

Because the number of boundary points to be inversed is comparatively large in this example, the basis function expansion should be considered to reduce the variables to be identified. Thereby, the influence of different polynomial basis function orders is first discussed in this case to guide the subsequent order selection. It can be seen from Table 5 that when the third-order polynomial is used, e_{L_2} can reach the magnitude of 10^{-5} and the maximum relative error is less than 0.02%. Therefore, the complete polynomial of third-order is adopted as the basis function of expansion in the following inversion processes.

(B) The effect of different measurement points.

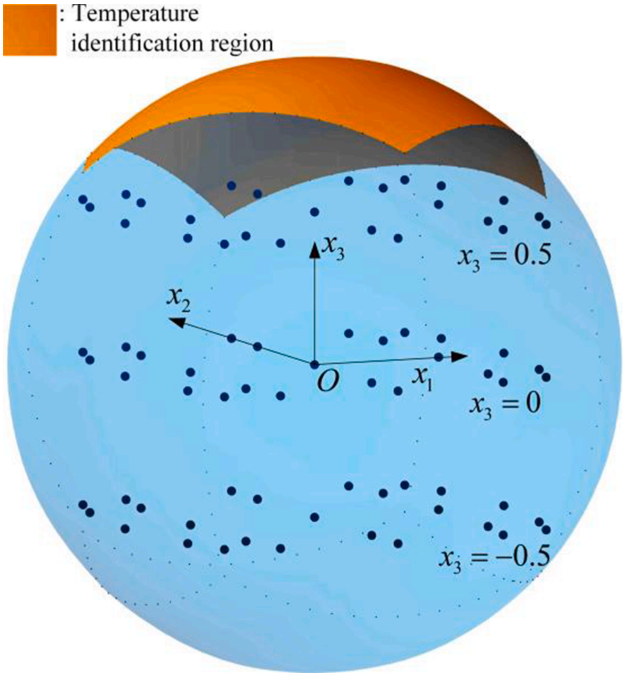

Fig. 12. Temperature region to be inversed and the distribution of measurement points of the sphere model.

Table 2
Temperature identification results at$t_{end} = 1$.

Measurement point positions	e_{L_2}	Mabserr	Mrelerr (%)
$x_3 = 0.5$	4.0628e-4	0.1023	0.0857
$x_3 = 0.0$	2.9494e-3	0.5253	0.5750
$x_3 = -0.5$	2.2498e-2	3.3537	4.0007

Table 3
The computational model information of fighter.

N_p	N_e	N_c	N_b	N_I
1102	1376	10,664	10,664	500

As shown in Fig. 17, four different numbers of measurement point distributions are considered.

It can be seen from Table 6 that too few measurement points will cause obvious oscillation of boundary condition identification results and lead to unacceptable inversion errors. But the error magnitude of e_{L_2} for 52 measuring points and hundreds of measuring points is10^{-5}. With the increase of the number of measuring points, the inversion results are slightly improved. Therefore, it is not advisable to use a too small number of measuring points in the process of solving the inverse problem. In order to take into account the accuracy and cost of the inversion, 104 measurement points as shown in Fig. 17 (b) are selected in the subsequent inversion process.

(C) The effect of different measurement errors.

In this case, considering the influence of measurement error on inversion results, the following error forms are introduced to simulate the real noise environment:

$$\widetilde{\boldsymbol{T}}_{um} = \widetilde{\boldsymbol{T}}'_{um} + \varepsilon\boldsymbol{\omega} \tag{62}$$

where $\widetilde{\boldsymbol{T}}'_{um}$ is the normalized temperature of measurement point obtained by the IG-DRBEM, ε denotes the deviation, $\boldsymbol{\omega}$ represents the random vector that belongs to [-1,1].

The ill-posedness of the inverse problem is caused by measurement error to a large extent, so it is a common technique to implement regularization. The classical Tikhonov regularization is used here to obtain stable inversion results. Therefore, when the temperature boundary conditions are inversed, the objective function Eq. (34) needs to be rewritten as.

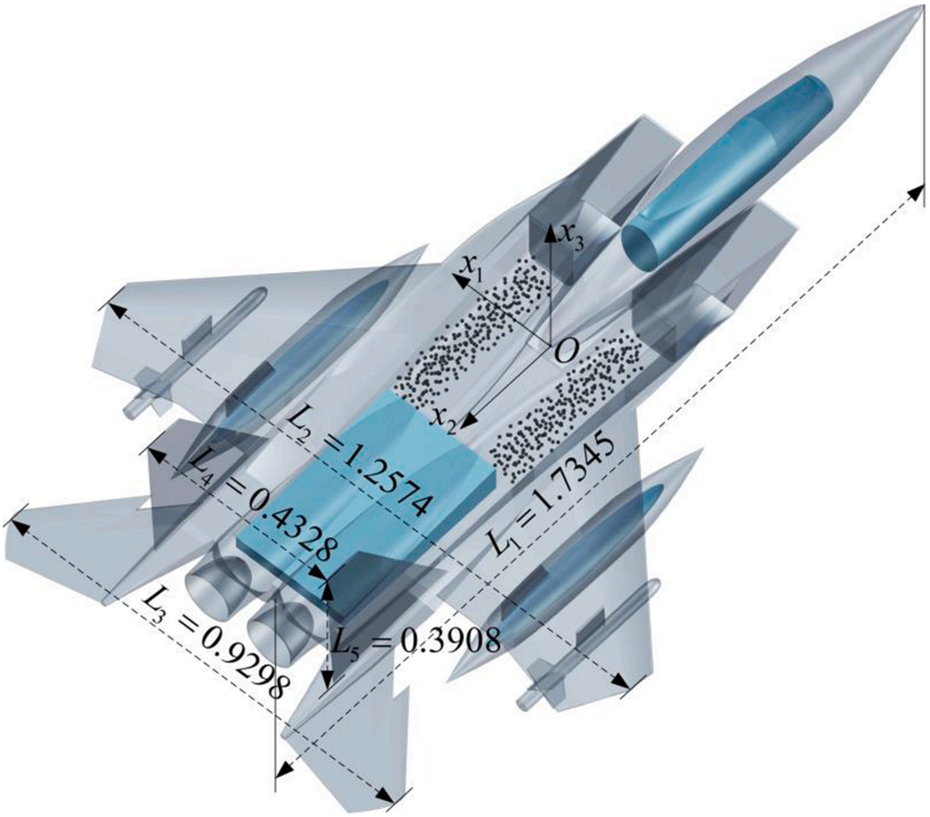

Fig. 13. The geometry model and the distribution of internal points. L1: the length of the fuselage; L2: the wingspan width of fighter; L3: the tailplane width of fighter; L4: the vertical tail spacing of fighter; L5: the vertical tail height of fighter.

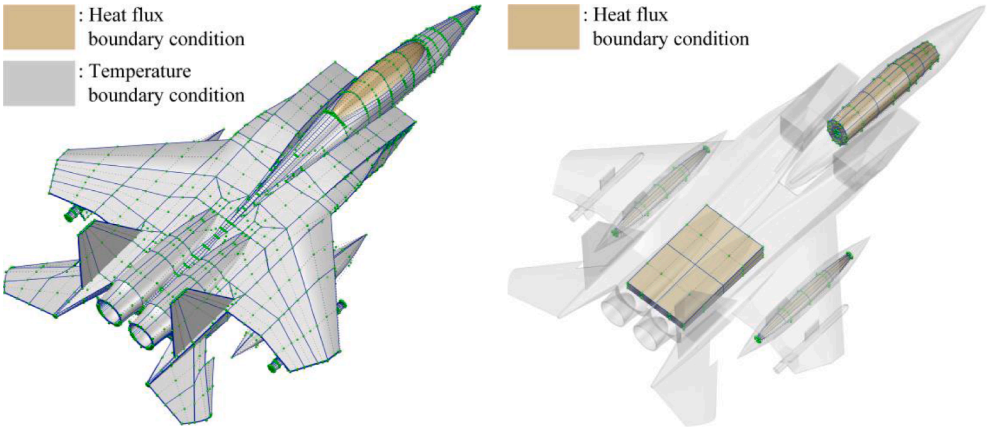

(a) Outer boundary (b) Inner boundary

Fig. 14. The distribution of control points and NURBS elements and the region position of imposing boundary conditions.

Table 4
Temperature results of all collocation points.

t	e_{L_2}	Mrelerr (%)
0.25	1.7024e-5	0.0353
0.50	1.7024e-5	0.0353
0.75	1.7024e-5	0.0353
1.00	1.7024e-5	0.0353

$$J = \left\| \widetilde{\boldsymbol{T}}_{ue}(t_{s+1}) - \widetilde{\boldsymbol{T}}_{um}(t_{s+1}) \right\|_2^2 + \lambda \| \boldsymbol{I}\boldsymbol{\alpha}(t_{s+1}) \|_2^2 \tag{63}$$

where λ represents the regularization parameter, and $\boldsymbol{I}$ denotes the identity matrix with the same dimension as the vector$\boldsymbol{\alpha}(t_{s+1})$.

Similar to the previous theory, by solving$\partial J / \partial \boldsymbol{\alpha}(t_{s+1}) = 0$, the optimal $\boldsymbol{\alpha}$ can be obtained as follows.

$$\boldsymbol{\alpha}(t_{s+1}) = \left(\breve{\boldsymbol{D}}^{\mathrm{T}} \breve{\boldsymbol{D}} + \lambda \boldsymbol{I} \right)^{-1} \breve{\boldsymbol{D}}^{\mathrm{T}} \left[\widetilde{\boldsymbol{T}}_{um}(t_{s+1}) - \boldsymbol{b}'_{e}(t_{s+1}) \right] \tag{64}$$

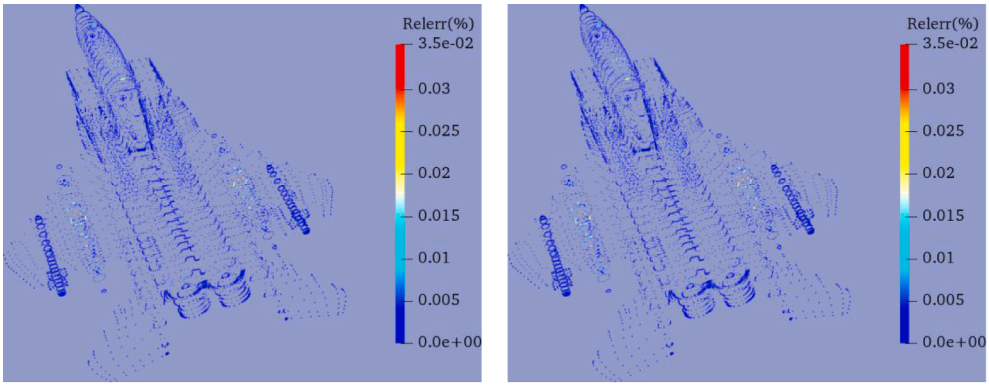

(a) $t = 0.25$ (b) $t = 0.5$

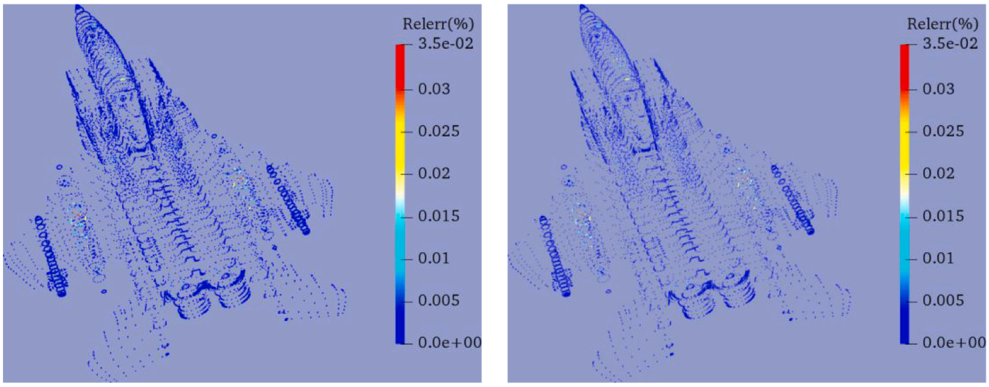

(c) $t = 0.75$ (d) $t = 1$

Fig. 15. The Relerr of temperature at all collocation points.

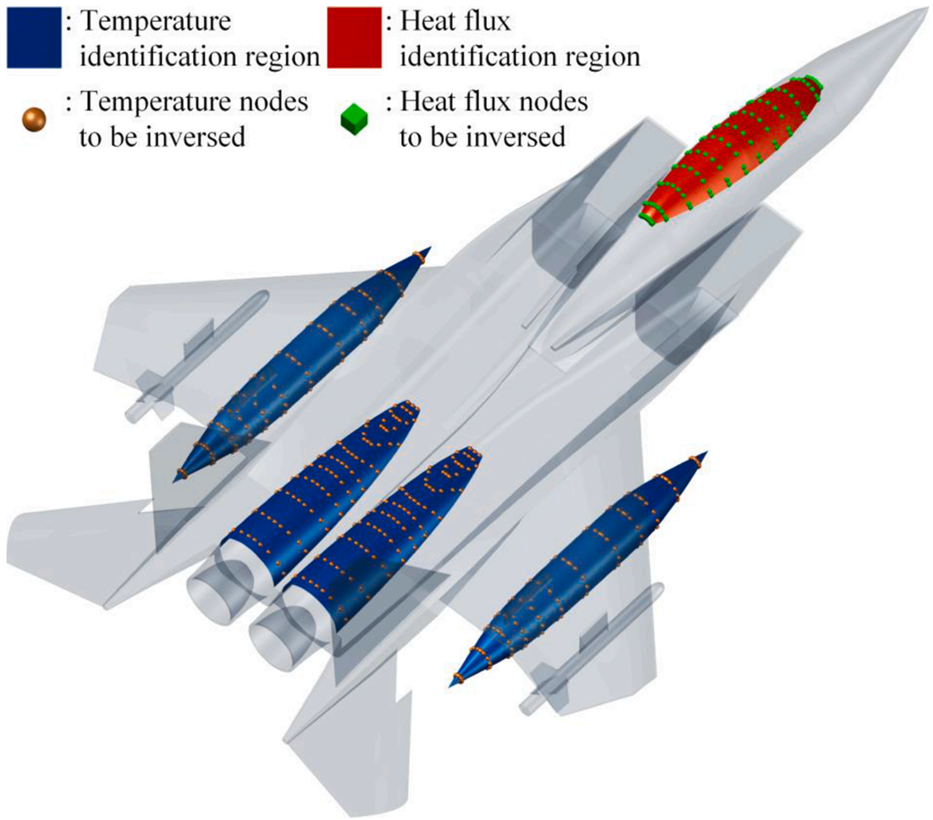

Fig. 16. Temperature and heat flux region to be inversed.

The effective selection of λ is an important prerequisite for obtaining stable and accurate$\boldsymbol{\alpha}^{(m+1)}(t_{m+1})$. Here, the generalized cross-validation (GCV) [59] is used to select the bestλ. This method constructs a function V about λ as follows.

$$V(\lambda) = \frac{\left\| \left(\boldsymbol{I} - \breve{\boldsymbol{D}} \left(\breve{\boldsymbol{D}}^{\mathrm{T}} \breve{\boldsymbol{D}} + \lambda \boldsymbol{I} \right)^{-1} \breve{\boldsymbol{D}}^{\mathrm{T}} \right) \left[\widetilde{\boldsymbol{T}}_{um}(t_{s+1}) - \boldsymbol{b}'_{e}(t_{s+1}) \right] \right\|_2^2}{\left(\mathrm{tr} \left[\boldsymbol{I} - \breve{\boldsymbol{D}} \left(\breve{\boldsymbol{D}}^{\mathrm{T}} \breve{\boldsymbol{D}} + \lambda \boldsymbol{I} \right)^{-1} \breve{\boldsymbol{D}}^{\mathrm{T}} \right] \right)^2} \tag{65}$$

where "tr" denotes the trace of the matrix. Here, when $V(\lambda)$ takes the minimum value, the corresponding λ is taken as the optimal regularization parameter value.

It is worth noting that although the ill condition of the matrix $\breve{\boldsymbol{D}}^{\mathrm{T}} \breve{\boldsymbol{D}}$ has been improved by implementing regularization, here we still use TSVD for matrix inversion.

In order to show the accuracy of inversion temperature boundary conditions and their influence on temperature distribution in other parts, several boundary points are added on each NURBS element on the body surface, and a total of 47,762 boundary points were added, as shown in Fig. 18. Fig. 19 shows the relative errors of temperature of all boundary collocation points calculated by using inversion temperature boundary conditions, where the reference solution is the unknown temperature obtained by using accurate boundary conditions. It can be seen that when random errors of 1%, 3% and 5% are adopted, the Mrelerr of temperature of all boundary collocation points does not exceed 0.082%, 0.19% and 0.23%, respectively. Therefore, the proposed method with the regularization scheme has good stability and high accuracy for inversion of temperature boundary conditions.

5.3.3. *The inversion of heat flux boundary conditions*

In this section, the inversion of the heat flux boundary condition is considered, and the region to be identified is OSUPC, where 96 collocation points are distributed, as shown in Fig. 16. The boundary condition type, physical parameters and heat source distribution applied to the whole body are consistent with Section 5.2.2. For example, the ISCCP, ISDT and ISCEP parts are adiabatic, and the OSUPC part is given a non-zero heat fluxq_{OSUPC}. The temperature boundary conditions of the rest parts of the body are given in accordance with Eq.. Also, the adopted expansion basis functions, the distribution scheme and number of measurement points are consistent with the conclusion in Section 5.2.2.

(A) Considering different heat flux expressions.

In this case,when q_{OSUPC} is a constant, linear, quadratic and trigonometric function, the inversion performance of the proposed method is considered, and the specific expression is as follows.

$$q_{OSUPC} = \begin{cases} 300 \\ 300(x_1 + x_2 + x_3 + 2)e^{-t} \\ 100\left(2x_1^2 + 3x_2^2 + 4x_3^2 + 5\right)e^{-t} \\ 100(\sin x_1 + \sin x_2 + \sin x_3 + 3)e^{-t} \end{cases} \tag{66}$$

It can be seen from Table 7 that the inversion method proposed in this paper has good stability and accuracy. For heat flux forms of different complexity, Mrelerr and e_{L_2} are respectively maintained at the same order of magnitude.

(B) The influence of different extent of measurement errors.

In this case, $q_{OSUPC} = 100\left(2x_1^2 + 3x_2^2 + 4x_3^2 + 5\right)e^{-t}$ is selected to investigate the influence of different measurement errors on the inversion results. Similar to the case (C) in Section 5.2.2, when the regularization scheme is adopted, the optimal in Eq. (44) can be modified as.

$$\boldsymbol{\alpha}(t_{s+1}) = \left(\widehat{\boldsymbol{D}}^{\mathrm{T}} \widehat{\boldsymbol{D}} + \lambda \boldsymbol{I} \right)^{-1} \widehat{\boldsymbol{D}}^{\mathrm{T}} \left[\widetilde{\boldsymbol{T}}_{um}(t_{s+1}) - \boldsymbol{b}_e(t_{s+1}) \right] \tag{67}$$

where the selection of λ and the computation of $\left(\widehat{\boldsymbol{D}}^{\mathrm{T}} \widehat{\boldsymbol{D}} + \lambda \boldsymbol{I} \right)^{-1}$ also adopted the GCV method and the TSVD, respectively.

The accuracy of the proposed inversion method has been demon-

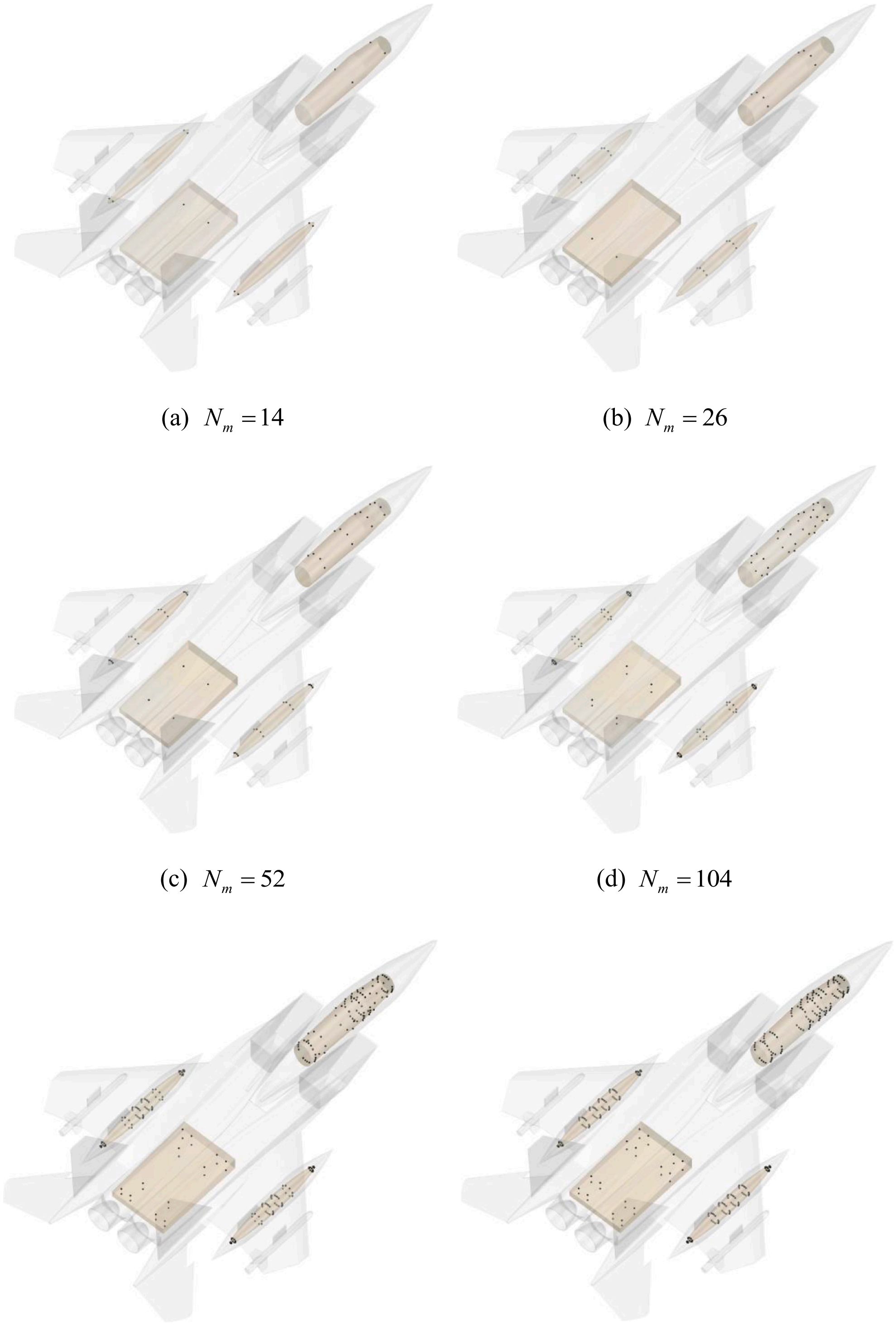

(a) $N_m = 14$ (b) $N_m = 26$

(c) $N_m = 52$ (d) $N_m = 104$

(e) $N_m = 312$ (f) $N_m = 416$

Fig. 17. The distribution of measurement points.

Table 5
Errors of inversion temperature boundary conditions with different expansion basis functions.

Polynomial orders	e_{L_2}	Mrelerr(%)
1	2.2851e-2	6.3516
2	5.1364e-4	0.1960
3	4.2770e-5	0.0152

Table 6
Errors of inversion temperature boundary conditions with differentN_m.

N_m	e_{L_2}	Mrelerr (%)
14	5.1631e-3	1.4836
26	4.0510e-3	0.9461
52	5.7538e-5	0.0166
104	4.2770e-5	0.0152
312	4.0880e-5	0.0135
416	4.0313e-5	0.0134

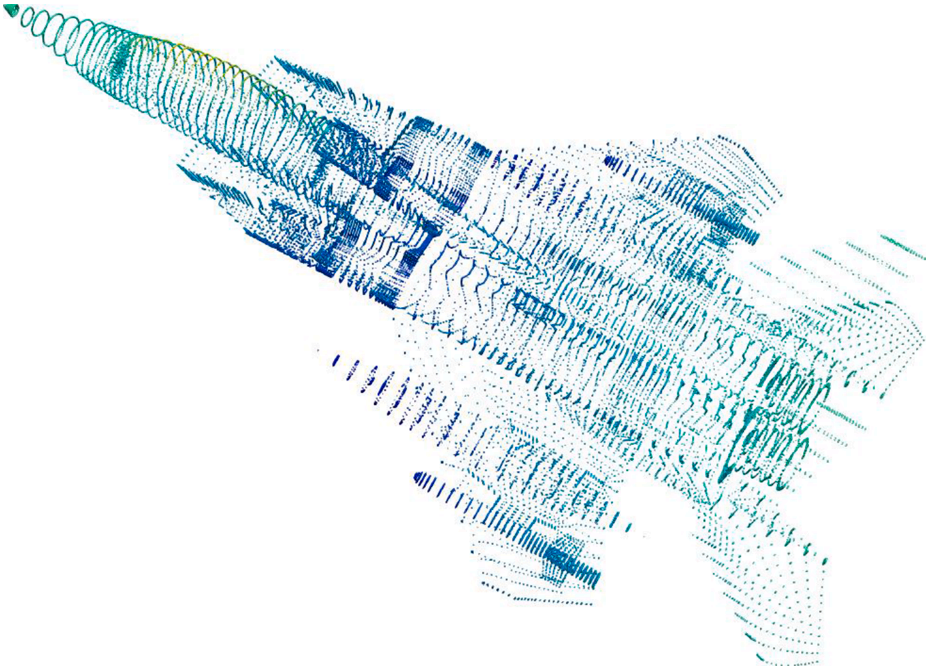

Fig. 18. Boundary points at the fighter including the boundary collocation points and the new added points in each NURBS element (BCP-NAP).

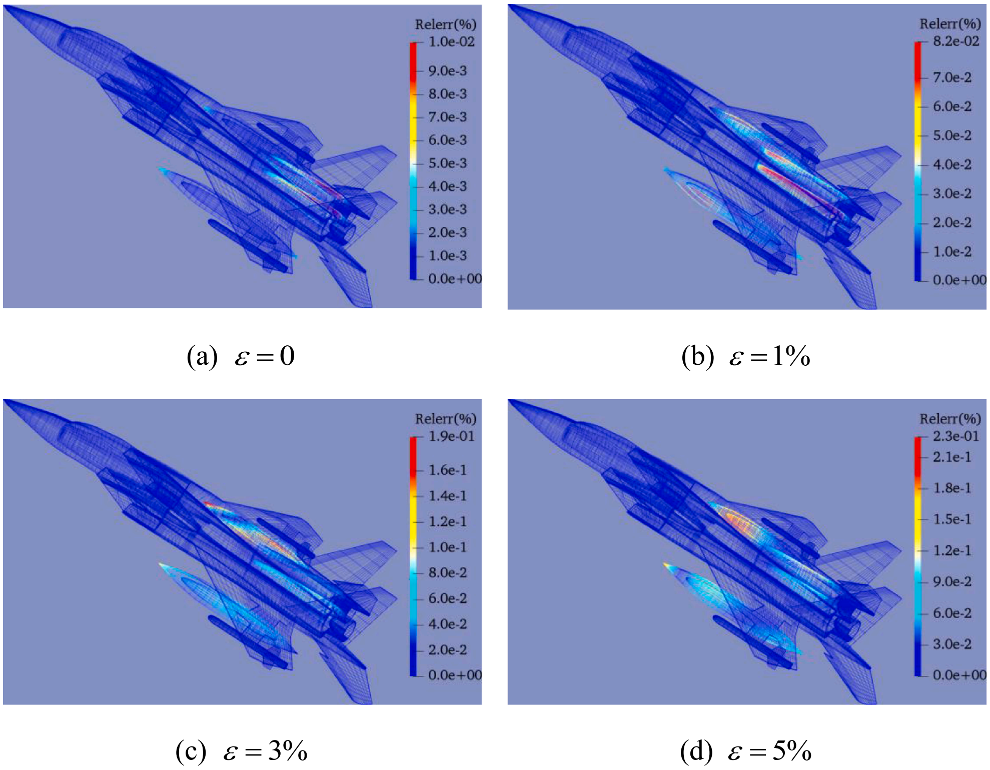

(a) $\varepsilon = 0$

(b) $\varepsilon = 1\%$

(c) $\varepsilon = 3\%$

(d) $\varepsilon = 5\%$

Fig. 19. Relerr of temperature of the BCP-NAP at $t = 1$ for inversing temperature boundary condition.

Table 7
Mrelerr and e_{L_2} of identifying heat flux with differentq_{OSUPC}.

q_{OSUPC}	e_{L_2}	Mrelerr (%)
Constant	1.9730e-6	5.8533e-4
Linear	3.2009e-6	9.0022e-4
Quadratic	3.6073e-6	9.0641e-4
Trigonometric	2.7547e-6	7.3439e-4

strated in case (A) in this Section for inversion of heat flux boundary conditions. Here, in order to intuitively reflect the influence of inversion heat flux boundary conditions on the temperature distribution of the fighter when different noises are considered, the temperature of the BCP-NAP is calculated. It can be seen from Fig. 20 that the presented inversion method can still obtain relatively stable and accurate temperature field distribution with different noises. Even when the error of $\varepsilon = 5\%$ is considered, the maximum relative error of the temperature

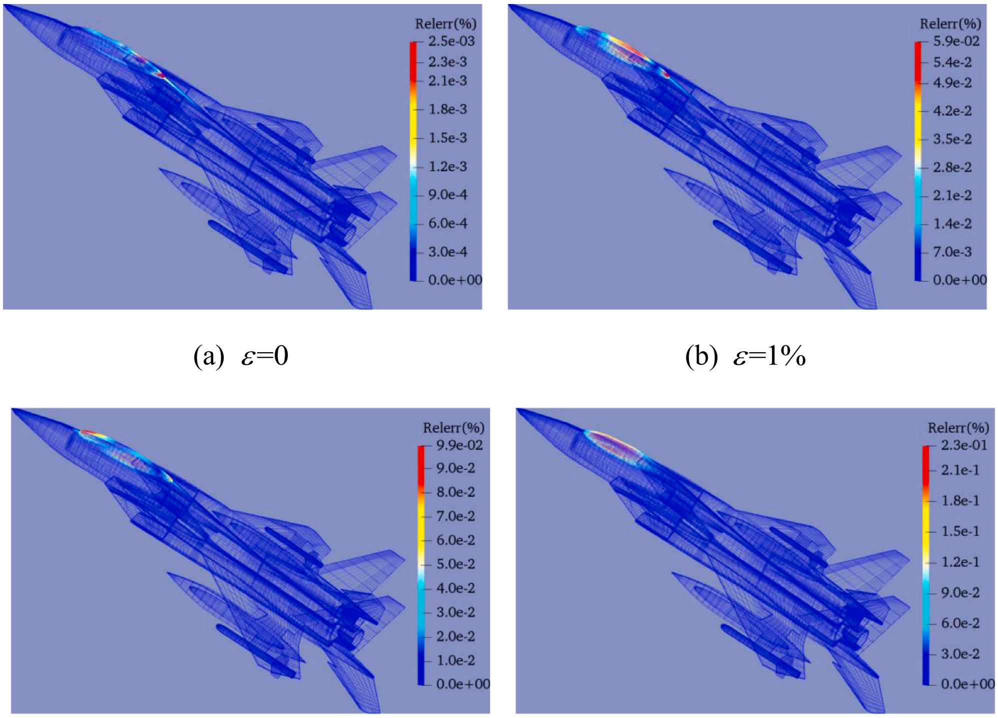

(a) ε=0

(b) ε=1%

(c) ε=3%

(d) ε=5%

Fig. 20. Relerr of temperature of the BCP-NAP at $t = 1$ for inversing heat flux boundary condition.

field obtained by using the inversed heat flux boundary conditions does not exceed 0.23%, and the reference solution is the temperature field obtained with the given analytical boundary conditions.

6. Conclusions

The contribution of this paper can be summarized into two parts. One is to establish a theoretical framework for IG-DRBEM to solve multi-patch models, which makes it possible for IG-DRBEM to analyze complex geometric problems. Meanwhile, the introduction of PIM enables IG-DRBEM to obtain stable time-domain results under different time steps, which advances the efficiency of IG-DRBEM in the analysis of transient problems. Another major innovative work is to propose a non-iterative inversion method for boundary condition identification based on the presented multi-patch analysis method, which further expands the research scope of IG-DRBEM. The realization of basis function expansion and regularization techniques further reduces the inversion dimension and promotes the anti-noise performance of the inversion method. The numerical examples systematically consider the influence of various factors on the inversion results. The results show that the proposed approach is not very sensitive to the influence of the number of measuring points. The inversion method can obtain relatively accurate inversion results, even under the influence of 5% random error, the Mrelerr is still less than 1%.

The assumed temperature field is only used to conveniently verify the effectiveness of the present methodology. In terms of practical problems, the main difficulties generally lie in the establishment of the geometric model, the imposition of boundary conditions, and the selection of location and number of measuring points. The proposed method's multi-patch computing capability and the high inversion accuracy under various boundary conditions, different distribution of measurement points and different extent of measurement errors prove that it is expected to have applicability for analyzing practical problems. Since the experimental conditions are not available at present, we will try experimental verification in the future, and then consider the practical application. Furthermore, the present method still has some shortcomings, such as (1) The main coefficient matrices in the solution system is asymmetric full matrices, so the computational efficiency may be inadequate when the problem scale is too large; (2) NURBS lacks the ability of local refinement because of the feature of the global tensor product and cannot perform the fine calculation on some critical parts of the geometry to be analyzed. In consideration of these factors, the T-spline or locally refined B-spline combined with the fast multipole method will be used to solve forward problems in the future. Simultaneously, other inverse analysis methods will be studied to solve more various inverse problems, thus further expanding the application of IG-DRBEM.

Declaration of Competing Interest

The authors declare that they have no known competing financial interests or personal relationships that could have appeared to influence the work reported in this paper.

Acknowledgement

The research was supported by the National Natural Science Foundation of China (No. 11872166), Foundation of State Key Laboratory of Structural Analysis of Industrial Equipment of China (No. GZ21109).

Appendix

(A) Constant approximation of $\boldsymbol{F}_u$

Assuming that $\boldsymbol{F}_u$ is the constant vector in any interval$[t_s,\ t_{s+1}]$, let.

$$\boldsymbol{F}_u(t_s+\tau)=\boldsymbol{F}_u(t_{s+1}) \tag{68}$$

Eq. (25) can be written as.

$$\widetilde{\boldsymbol{T}}_u(t_{s+1})=\widehat{\boldsymbol{E}}\left[\widetilde{\boldsymbol{T}}_u(t_s)+\boldsymbol{B}^{-1}\boldsymbol{F}_u(t_{s+1})\right]-\boldsymbol{B}^{-1}\boldsymbol{F}_u(t_{s+1}) \tag{69}$$

(B) Linear approximation of $\boldsymbol{F}_u$

Assuming that $\boldsymbol{F}_u$ varies linearly on any interval$[t_s,\ t_{s+1}]$, let.

$$\boldsymbol{F}_u(t_s+\tau)=\boldsymbol{r}_0+\boldsymbol{r}_1\cdot\tau \tag{70}$$

where.

$$\begin{aligned}\boldsymbol{r}_0&=\boldsymbol{F}_u(t_s)\\ \boldsymbol{r}_1&=\frac{1}{\Delta t}\left[\boldsymbol{F}_u(t_{s+1})-\boldsymbol{r}_0\right]\end{aligned} \tag{71}$$

Eq. (25) can be written as.

$$\widetilde{\boldsymbol{T}}_u(t_{s+1})=\widehat{\boldsymbol{E}}\left[\widetilde{\boldsymbol{T}}_u(t_s)+\boldsymbol{B}^{-1}\left(\boldsymbol{r}_0+\boldsymbol{B}^{-1}\boldsymbol{r}_1\right)\right]-\boldsymbol{B}^{-1}\left(\boldsymbol{r}_0+\boldsymbol{B}^{-1}\boldsymbol{r}_1+\Delta t\boldsymbol{r}_1\right) \tag{72}$$

(C) Quadratic approximation of $\boldsymbol{F}_u$

Using quadratic function to approximate$\boldsymbol{F}_u$, it is given by.

$$\boldsymbol{F}_u(t_s+\tau)=\boldsymbol{r}_0+\boldsymbol{r}_1\tau+\boldsymbol{r}_2\tau^2 \tag{73}$$

where.

$$\begin{cases}\boldsymbol{r}_0=\boldsymbol{F}_u(t_s)\\ \boldsymbol{r}_1=-\dfrac{1}{\Delta t}\left(3\boldsymbol{F}_u(t_s)-4\boldsymbol{F}_u(t_s+\dfrac{\Delta t}{2})+\boldsymbol{F}_u(t_{s+1})\right)\\ \boldsymbol{r}_2=\dfrac{2}{\Delta t^2}\left(\boldsymbol{F}_u(t_s)-2\boldsymbol{F}_u(t_s+\dfrac{\Delta t}{2})+\boldsymbol{F}_u(t_{s+1})\right)\end{cases} \tag{74}$$

Then, Eq. (25) can be integrated as.

$$\widetilde{\boldsymbol{T}}_u(t_{s+1})=\widehat{\boldsymbol{E}}\widetilde{\boldsymbol{T}}_u(t_s)+\boldsymbol{A}\boldsymbol{r}_0+\boldsymbol{A}_1\boldsymbol{r}_1+\boldsymbol{A}_2\boldsymbol{r}_2 \tag{75}$$

where.

$$\begin{cases}\boldsymbol{A}=\widehat{\boldsymbol{E}}\boldsymbol{B}^{-1}-\boldsymbol{B}^{-1}\\ \boldsymbol{A}_1=\widehat{\boldsymbol{E}}\left(\boldsymbol{B}^{-1}\right)^2-\left(\boldsymbol{B}^{-1}\right)^2-\Delta t\boldsymbol{B}^{-1}\\ \boldsymbol{A}_2=2\widehat{\boldsymbol{E}}\left(\boldsymbol{B}^{-1}\right)^3-2\Delta t\left(\boldsymbol{B}^{-1}\right)^2-2\left(\boldsymbol{B}^{-1}\right)^3-\Delta t^2\boldsymbol{B}^{-1}\end{cases} \tag{76}$$

References

[1] T.J.R. Hughes, J.A. Cottrell, Y. Bazilevs, Isogeometric analysis: CAD, finite elements, NURBS, exact geometry and mesh refinement, Comput. Methods Appl. Mech. Engrg. 194 (39–41) (2005) 4135–4195.

[2] M.J. Borden, M.A. Scott, J.A. Evans, T.J.R. Hughes, Isogeometric finite element data structures based on Bézier extraction of NURBS, Int. J. Numer. Methods Eng. 87 (1–5) (2011) 15–47.

[3] X. Wang, X.F. Zhu, P. Hu, Isogeometric finite element method for buckling analysis of generally laminated composite beams with different boundary conditions, Int. J. Mech. Sci. 104 (2015) 190–199.

[4] H.A. Jahangiry, A. Jahangiri, Combination of Isogeometric analysis and level-set method in topology optimization of heat-conduction systems, Appl. Therm. Eng. 161 (2019), 114134.

[5] F. Auricchio, L.B. Da Veiga, T.J.R. Hughes, A. Reali, G. Sangalli, Isogeometric collocation methods, Math. Models Meth. Appl. Sci. 20 (11) (2010) 2075–2107.

[6] P. Fedeli, A. Frangi, F. Auricchio, A. Reali, Phase-field modeling for polarization evolution in ferroelectric materials via an isogeometric collocation method, Comput. Methods Appl. Mech. Engrg. 351 (2019) 789–807.

[7] R.N. Simpson, S.P.A. Bordas, J. Trevelyan, T. Rabczuk, A two-dimensional isogeometric boundary element method for elastostatic analysis, Comput. Methods Appl. Mech. Engrg. 209 (2012) 87–100.

[8] L.L. Chen, H. Lian, Z. Liu, H.B. Chen, E. Atroshchenko, S.P.A. Bordas, Structural shape optimization of three dimensional acoustic problems with isogeometric boundary element methods, Comput. Methods Appl. Mech. Engrg. 355 (2019) 926–951.

[9] A. Borković, G. Radenković, D. Majstorović, S. Milovanovic, D. Milasinovic, R. Cvijic, Free vibration analysis of singly curved shells using the isogeometric finite strip method, Thin-Walled Struct. 157 (2020), 107125.

[10] R.N. Simpson, S.P.A. Bordas, H. Lian, J. Trevelyan, An isogeometric boundary element method for elastostatic analysis: 2D implementation aspects, Comput. Struct. 118 (2013) 2–12.

[11] M.A. Scott, R.N. Simpson, J.A. Evans, S. Lipton, S.P.A. Bordas, T.J.R. Hughes, T. W. Sederberg, Isogeometric boundary element analysis using unstructured T-splines, Comput. Methods Appl. Mech. Engrg. 254 (2013) 197–221.
[12] R.N. Simpson, M.A. Scott, M. Taus, D.C. Thomas, H. Lian, Acoustic isogeometric boundary element analysis, Comput. Methods Appl. Mech. Engrg. 269 (2014) 265–290.
[13] M.J. Peake, J. Trevelyan, G. Coates, Extended isogeometric boundary element method (XIBEM) for three-dimensional medium-wave acoustic scattering problems, Comput. Methods Appl. Mech. Engrg. 284 (2015) 762–780.
[14] J.V. Venås, T. Kvamsdal, Isogeometric boundary element method for acoustic scattering by a submarine, Comput. Methods Appl. Mech. Engrg. 359 (2020), 112670.
[15] Y.P. Gong, C.Y. Dong, X.C. Qin, An isogeometric boundary element method for three dimensional potential problems, J. Comput. Appl. Math. 313 (2017) 454–468.
[16] G. Beer, C. Duenser, Isogeometric boundary element analysis of problems in potential flow, Comput. Methods Appl. Mech. Engrg. 347 (2019) 517–532.
[17] R.N. Simpson, Z. Liu, R. Vazquez, J.A. Evans, An isogeometric boundary element method for electromagnetic scattering with compatible B-spline discretizations, J. Comput. Phys. 362 (2018) 264–289.
[18] J. Dölz, S. Kurz, S. Schöps, F. Wolf, Isogeometric boundary elements in electromagnetism: rigorous analysis, fast methods, and examples, SIAM J. Sci. Comput. 41 (5) (2019).
[19] Z.L. An, T.T. Yu, T.Q. Bui, C. Wang, N.A. Trinh, Implementation of isogeometric boundary element method for 2-D steady heat transfer analysis, Adv. Eng. Softw. 116 (2018) 36–49.
[20] X. Peng, E. Atroshchenko, P. Kerfriden, S.P.A. Bordas, Isogeometric boundary element methods for three dimensional static fracture and fatigue crack growth, Comput. Methods Appl. Mech. Engrg. 316 (2017) 151–185.
[21] F.L. Sun, C.Y. Dong, H.S. Yang, Isogeometric boundary element method for crack propagation based on Bézier extraction of NURBS, Eng. Anal. Bound. Elem. 99 (2019) 76–88.
[22] H. Lian, P. Kerfriden, S.P.A. Bordas, Shape optimization directly from CAD: An isogeometric boundary element approach using T-splines, Comput. Methods Appl. Mech. Engrg. 317 (2017) 1–41.
[23] M. Yoon, J. Lee, B. Koo, Shape design optimization of thermoelasticity problems using isogeometric boundary element method, Adv. Eng. Softw. 149 (2020), 102871.
[24] G. Beer, B. Marussig, J. Zechner, C. Dünser, T.P. Fries, Isogeometric boundary element analysis with elasto-plastic inclusions. Part 1: plane problems, Comput. Methods Appl. Mech. Engrg. 308 (2016) 552–570.
[25] H.L. Oliveira, H.d.C.e. Andrade, E.D. Leonel, An isogeometric boundary element approach for topology optimization using the level set method, Appl. Math. Model. 84 (2020) 536–553.
[26] F.H. Jiang, W.C. Zhao, L.L. Chen, C.J. Zheng, H.B. Chen, Combined shape and topology optimization for sound barrier by using the isogeometric boundary element method, Eng. Anal. Bound. Elem. 124 (2021) 124–136.
[27] W.H. Fang, Z.L. An, T.T. Yu, T.Q. Bui, Isogeometric boundary element analysis for two-dimensional thermoelasticity with variable temperature, Eng. Anal. Bound. Elem. 110 (2020) 80–94.
[28] B. Yu, G.Y. Cao, W.D. Huo, H.L. Zhou, E. Atroshchenko, Isogeometric dual reciprocity boundary element method for solving transient heat conduction problems with heat sources, J. Comput. Appl. Math. 385 (2021), 113197.
[29] C. Xu, C. Dong, R. Dai, RI-IGABEM based on PIM in transient heat conduction problems of FGMs, Comput. Methods Appl. Mech. Engrg. 374 (2021) 113601.
[30] V.P. Nguyen, P. Kerfriden, M. Brino, S.P.A. Bordas, E. Bonisoli, Nitsche's method for two and three dimensional NURBS patch coupling, Comput. Mech. 53 (6) (2014) 1163–1182.
[31] J.M. Gu, T.T. Yu, L.V. Nguyen, T.T. Lich, T.Q.B. Nguyen, Adaptive multi-patch isogeometric analysis based on locally refined B-splines, Comput. Methods Appl. Mech. Engrg. 339 (2018) 704–738.
[32] M. Ruess, D. Schillinger, A.I. Oezcan, E. Rank, Weak coupling for isogeometric analysis of non-matching and trimmed multi-patch geometries, Comput. Methods Appl. Mech. Engrg. 269 (2014) 46–71.
[33] S. Kargaran, B. Jüttler, S.K. Kleiss, A. Mantzaflaris, T. Takacs, Overlapping multi-patch structures in isogeometric analysis, Comput. Methods Appl. Mech. Engrg. 356 (2019) 325–353.
[34] Y.J. Wang, D.J. Benson, A.P. Nagy, A multi-patch nonsingular isogeometric boundary element method using trimmed elements, Comput. Mech. 56 (1) (2015) 173–191.
[35] Y.J. Wang, D.J. Benson, Multi-patch nonsingular isogeometric boundary element analysis in 3D, Comput. Methods Appl. Mech. Engrg. 293 (2015) 71–91.
[36] B. Yu, G.Y. Cao, Z. Meng, Y.P. Gong, C.Y. Dong, Three-dimensional transient heat conduction problems in FGMs via IG-DRBEM, Comput. Methods Appl. Mech. Engrg. 384 (2021), 113958.
[37] B. Yu, W.A. Yao, Q. Gao, A precise integration boundary element method for solving transient heat conduction problems with variable thermal conductivity, Numer Heat Tranf. B-Fundam. 65 (5) (2014) 472–493.
[38] P.W. Partridge, C.A. Brebbia, L.C. Wrobel (Eds.), The Dual Reciprocity Boundary Element Method, Springer Netherlands, Dordrecht, 1991.
[39] M.E. Yildizdag, I.T. Ardic, A. Kefal, A. Ergin, An isogeometric FE-BE method and experimental investigation for the hydroelastic analysis of a horizontal circular cylindrical shell partially filled with fluid, Thin-Walled Struct. 151 (2020), 106755.
[40] A. Kefal, E. Oterkus, Isogeometric iFEM analysis of thin shell structures, Sensors 20 (9) (2020) 2685.
[41] A. Kefal, I.E. Tabrizi, M. Yildiz, A. Tessler, A smoothed iFEM approach for efficient shape-sensing applications: Numerical and experimental validation on composite structures, Mech. Syst. Signal Proc. 152 (2021) 107486.
[42] F.F. Zhao, H. Bao, An improved inverse finite element method for shape sensing using isogeometric analysis, Measurement 167 (2021), 108282.
[43] F.F. Zhao, H. Bao, J.F. Liu J, K.X. Li, Shape sensing of multilayered composite and sandwich beams based on Refined Zigzag Theory and inverse finite element method, Compos. Struct. 261 (2021) 113321.
[44] C.H. Huang, C.C. Shih, A shape identification problem in estimating simultaneously two interfacial configurations in a multiple region domain, Appl. Therm. Eng. 26 (1) (2006) 77–88.
[45] M. Cui, J. Mei, B.W. Zhang, B.B. Xu, L. Zhou, Y.W. Zhang, Inverse identification of boundary conditions in a scramjet combustor with a regenerative cooling system, Appl. Therm. Eng. 134 (2018) 555–563.
[46] H.L. Chen, B. Yu, H.L. Zhou, Z. Meng, Identification of transient boundary conditions with improved cuckoo search algorithm and polynomial approximation, Eng. Anal. Bound. Elem. 95 (2018) 124–141.
[47] Z.X. Zhao, M.K. Banda, B.Z. Guo, Simultaneous identification of diffusion coefficient, spacewise dependent source and initial value for one-dimensional heat equation, Math. Meth. Appl. Sci. 40 (10) (2017) 3552–3565.
[48] V. Tahmasbi, S. Noori, Inverse identification of temperature-dependent thermal conductivity coefficients in an orthotropic charring composite, Appl. Therm. Eng. 183 (2021), 116219.
[49] J.H. Huang, V.T. Than, T.T. Ngo, C.C. Wang, An inverse method for estimating heat sources in a high speed spindle, Appl. Therm. Eng. 105 (2016) 65–76.
[50] S. Kumar, S.P. Mahulikar, Reconstruction of aero-thermal heating and thermal protection material response of a Reusable Launch Vehicle using inverse method, Appl. Therm. Eng. 103 (2016) 344–355.
[51] Y.B. Liu, X.S. Wang, X.Y. Meng, D.W. Wang, A review on tube external heat transfer for passive residual heat removal heat exchanger in nuclear power plant, Appl. Therm. Eng. 149 (2019) 1476–1491.
[52] A. Tamburrino, G. Rubinacci, A new non-iterative inversion method for electrical resistance tomography, Inverse Probl. 18 (6) (2002) 1809–1829.
[53] X.W. Ling, R.G. Keanini, H.P. Cherukuri, A non-iterative finite element method for inverse heat conduction problems, Int. J. Numer. Methods Eng. 56 (9) (2003) 1315–1334.
[54] B. Yu, W.A. Yao, Q. Gao, H.L. Zhou, C. Xu, A novel non-iterative inverse method for estimating boundary condition of the furnace inner wall, Int. Commun. Heat Mass Transf. 87 (2017) 91–97.
[55] B. Yu, C. Xu, H.L. Zhou, M. Cui, A novel non-iterative method for estimating boundary conditions and geometry of furnace inner wall made of FGMs, Appl. Therm. Eng. 147 (2019) 251–271.
[56] B.S. Chen, L.Y. Tong, Y.X. Gu, H.W. Zhang, O. Ochoa, Transient heat transfer analysis of functionally graded materials using adaptive precise time integration and graded finite elements, Numer. Heat Tranf. B-Fundam. 45 (2) (2004) 181–200.
[57] B. Yu, W.A. Yao, Q. Gao, Adaptive Precise Integration BEM for Solving Transient Heat Conduction Problems, International Conference on Computational Methods 1, ISSN 2374-3948.
[58] B. Yu, W.A. Yao, A precise time-domain expanding boundary-element method for solving three-dimensional transient heat conduction problems with variable thermal conductivity, Numer Heat Tranf. B-Fundam. 66 (5) (2014) 422–445.
[59] G.H. Golub, M. Heath, G. Wahba, Generalized cross-validation as a method for choosing a good ridge parameter, Technometrics 21 (2) (1979) 215–223.